Economic Geology, v. 110, pp. 889–923

Porphyry to Epithermal Transition in the Altar Cu-(Au-Mo) Deposit, Argentina, Studied by Cathodoluminescence, LA-ICP-MS, and Fluid Inclusion Analysis

Laura Maydagán,[1,†] Marta Franchini,[2,3] Brian Rusk,[4] David R. Lentz,[5] Christopher McFarlane,[5] Agnes Impiccini,[3] Francisco Javier Ríos,[6] and Roger Rey[7]

[1] *Centro Patagónico de Estudios Metalogenéticos-CONICET-INGEOSUR, Departamento de Geología, Universidad Nacional del Sur, San Juan 670, 8000 Bahía Blanca, Argentina*

[2] *Centro Patagónico de Estudios Metalogenéticos-CONICET, Instituto de Investigación en Paleobiología y Geología, Universidad Nacional de Río Negro, Av. Roca 1242, 8332 Roca, Argentina*

[3] *Departamento de Geología y Petróleo, Facultad de Ingeniería, Universidad Nacional del Comahue, Buenos Aires 1400, 8300 Neuquén, Argentina*

[4] *Department of Geology, Western Washington University, Bellingham, Washington, USA*

[5] *Department of Earth Sciences, University of New Brunswick, Fredericton, New Brunswick E3B 5A3, Canada*

[6] *Centro de Desenvolvimiento da Tecnologia Nuclear, CNEN, CxPs 941- Belo Horizonte, Brazil*

[7] *Minera Peregrine Argentina S.A, Santa Fe (Oeste) 117, Piso 5, Edificio Derby, Ciudad San Juan, Argentina*

Abstract

The middle to late Miocene Altar porphyry Cu-(Au-Mo) deposit, located in the Andean Main Cordillera of San Juan Province (Argentina), is characterized by the superposition of multiple vein generations consisting of both porphyry-type and high sulfidation epithermal-style alteration and mineralization. We constrain the physical and chemical evolution of the hydrothermal fluids that formed this deposit based on description and distribution of vein types, scanning electron microscopy, cathodoluminescence (CL) imaging, trace elements in quartz veins, and fluid inclusion microthermometry.

Quartz CL textures and trace elements (chiefly Li, Al, Ti, and Ge) differentiate among quartz generations precipitated during different mineralization and alteration events. Early quartz ± chalcopyrite ± pyrite veins and quartz ± molybdenite veins (A and B veins) show considerable complexity and were commonly reopened, and some underwent quartz dissolution. Early quartz ± chalcopyrite ± pyrite veins (A veins) are dominated by equigranular bright CL quartz with homogeneous texture. Most of these veins contain higher Ti concentrations than any other vein type (average: 100 ppm) and have low to intermediate Al concentrations (65–448 ppm). Quartz ± molybdenite (B veins) and chlorite + rutile ± hematite (C veins) veins contain quartz of intermediate CL intensity that commonly shows growth zones with oscillatory CL intensity. Quartz from these veins has intermediate Ti concentrations (~20 ppm) and Al concentrations similar to those of A veins. Quartz from later quartz + pyrite veins with quartz + muscovite ± tourmaline halos (D veins) has significantly lower CL intensity, low Ti (<15 ppm) and elevated Al concentrations (up to 1,000 ppm), and typically contains euhedral growth zones. Late veins rich in sulfides and sulfosalts show CL textures typical of epithermal deposits (dark CL quartz, crustiform banding, and euhedral growth zones). Quartz from these veins typically contains less than 5 ppm Ti, and Al, Li, and Ge concentrations are elevated relative to other vein types. Based on experimentally established relationships between Ti concentration in quartz and temperature, the decrease in Ti content in successively later quartz generations indicates that the temperature of the hydrothermal fluids decreased through time during the evolution of the system.

Vein formation at Altar occurred at progressively lower pressure, shallower paleodepth, and lower temperature. Under lithostatic pressures, the magma supplied low-salinity aqueous fluids at depths of ~6 to 6.8 km (pressures of 1.6–1.8 kbar) and temperatures of 670° to 730°C (first quartz generation of early quartz ± chalcopyrite ± pyrite veins). This parental fluid episodically depressurized and cooled at temperatures and pressures below the brine-vapor solvus. Quartz ± molybdenite veins precipitated from fluids at temperatures of 510° to 540°C and pressures of 800 to 1,000 bars, corresponding to depths of 3 to 3.7 km under lithostatic pressures. Further cooling of hydrothermal fluids to temperatures between 425° and 370°C under hydrostatic pressures of 200 to 350 bars produced pyrite-quartz veins and pervasive quartz + muscovite ± tourmaline and illite alteration that overprinted the early hydrothermal assemblages. Late veins rich in sulfides and sulfosalts that overlapped the deep and intermediate high-temperature veins formed from fluids at temperatures of 250° to 280°C and pressures of 20 to 150 bars. The epithermal siliceous ledges formed from low-temperature fluids (<230°C) at hydrostatic pressures of <100 bars corresponding to depths of <<1 km.

Introduction

Porphyry-Cu (Mo-Au) and high sulfidation epithermal-style ore deposits constitute major global resources of precious and base metals (e.g., Seedorff et al., 2005). These deposits form in convergent tectonic regimes associated with calc-alkaline to alkaline magmatism and typically exhibit close spatial and temporal relationships to one another (Sillitoe, 1983; Arribas et al., 1995). Evidence for a close genetic relationship

† Corresponding author: e-mail, lauramaydagan@yahoo.com.ar

Submitted: March 6, 2013
Accepted: October 14, 2014

between porphyry- and epithermal-style mineralization has been documented in numerous ore districts including Butte, Chuquicamata, Lepanto Far South East, Baguio, Agua Rica, and others (e.g., Hedenquist et al., 1998; Muntean and Einaudi, 2001; Ossandón et al., 2001; Heinrich, 2005; Rusk et al., 2008b; Cooke et al., 2011; Deyell and Hedenquist, 2011; Franchini et al., 2011, 2012; Catchpole et al., 2012). Even where a genetic relationship is clear between porphyry and epithermal mineralization, the physical and chemical evolution of the hydrothermal system that accompanies the transition from porphyry to epithermal mineralization warrants further investigation (e.g., Gammons and Williams Jones, 1997; Muntean and Einaudi, 2001; Sillitoe and Hedenquist, 2003; Heinrich et al., 2004).

Understanding the evolution of the pressure, temperature, and fluid conditions during porphyry and subsequent epithermal mineralization is complicated by the fact that these deposits are characterized by superposition of multiple mineralization events that take place under different pressure and temperature conditions. Such superposition typically results in progressively cooler vein mineralization assemblages crosscutting older and hotter vein and alteration assemblages. Reopening of older veins by later veins is common but can be difficult to infer based on field relations and hand sample observations.

The Altar porphyry Cu (Au-Mo) and associated epithermal deposits in the Andean Main Cordillera of San Juan Province (31º29'S, 70º28'W), Argentina, is an excellent example of a deposit containing both porphyry Cu (Mo-Au) mineralization and related high sulfidation epithermal Au mineralization. The Altar ore deposits formed during several magmatic and hydrothermal pulses in the middle to late Miocene. Laser ablation-inductively coupled plasma-mass spectrometry (LA-ICP-MS) U-Pb ages of zircons from the Altar porphyries indicate four discrete intrusion events over an extended magmatic life of ca. 3 m.y. (Maydagán et al., 2014). The complex superposition of multiple vein, mineralization, and alteration events at Altar makes it difficult to decipher the evolving pressure, temperature, and fluid composition of the deposit, and the relationships between mineralization and alteration are commonly obscured. Cathodoluminescence (CL) is a powerful tool to deconvolute the sequence of mineralizing events and relationships between quartz and ore minerals (e.g., Rusk and Reed, 2002; Müller et al., 2003). CL textures provide the context necessary to relate fluid inclusion, isotopic, or mineral trace element studies to specific mineralization events. When these techniques are integrated, they elucidate the progressive changes in fluid pressure, temperature, and composition throughout the life of the hydrothermal system (Rusk et al., 2006; Allan and Yardley, 2007; Müller et al., 2010).

In this study, we systematically investigate the CL textures and quartz trace elements from all identified vein generations that formed the Altar hydrothermal system, from the earliest to latest veins of the porphyry deposit to the late epithermal siliceous ledges. The results show that CL textures and quartz trace elements differentiate between mineralization events, such that each vein generation has a unique quartz trace element signature, which can be visualized using CL. The combined thermobarometry derived from Ti-in-quartz compositions from each vein generation (e.g., Thomas et al., 2010; Huang and Audétat, 2012), together with fluid inclusion microthermometric and thermobarometric data, reveals the progressive changes in pressure and temperature that accompanied vein formation throughout the entire magmatic-hydrothermal history of the hydrothermal system that formed the Altar porphyry and epithermal deposits.

Regional Tectonic and Geologic Setting

The Altar region is located in the Andean Main Cordillera over the flat-slab segment (27°–33° S) of the southern Central Andes. The subducting slab in this segment has a relatively smooth transition to the north, toward the Central volcanic zone, and a southerly transition to segments with a steeper subduction angle (30°; Cahill and Isacks, 1992; Anderson et al., 2007; Gans et al., 2011). From 35 to 21 Ma, in the western part of the Cordillera Principal between 32° and 37° S, thick volcanosedimentary sequences accumulated under an extensional tectonic regime (Charrier et al., 2002) in volcanotectonic depressions or intra-arc basins, which in the study region is the Abanico basin (Muñoz et al., 2006; Mpodozis and Cornejo, 2012; Fig. 1A). These sequences were assigned to Abanico, Coya-Machalí, and Cura-Mallín formations (e.g., Jordan et al., 2001; Charrier et al., 2002; Kay et al., 2005; Farías et al., 2008). During the early Miocene (27–20 Ma), this segment had a subducted slab geometry similar to that currently observed in the normal-slab segment at 35°S and a crustal thickness of 35 to 40 km (Kay and Mpodozis, 2002). The shallowing of the subduction zone progressed from middle to late Miocene (20–5 Ma), accompanied by the subduction of the Juan Fernández ridge (e.g., Yáñez et al., 2001) and eastward migration and broadening of the arc (Kay and Mpodozis, 2002). The emplacement of the porphyries took place under a compressive regime and crustal shortening. Basin inversion and significant tectonic uplift of the Principal Andean Cordillera occurred as a result of the Neogene compressive tectonism (Maksaev et al., 2009). Cessation of the magmatic activity over the flat-slab Miocene arc occurred at 5 Ma. Subsequent magmatism over the flat slab was present in the back arc, in particular the Farallón Negro, Pocho, and San Luis magmatic centers (Kay and Mpodozis, 2002).

Exploration History and Local Geology

The Altar area was poorly known geologically until 1995, when CRA Exploration Argentina outlined a broad zone of alteration and mineralization. The project was explored by Rio Tinto Mining and Exploration (1999–2003) and Peregrine Metals Ltd. (2005–2011). In 2011, Stillwater Mining Company completed the acquisition of Peregrine Metals Ltd. and the Altar project and created Minera Peregrine Argentina S.A. The Altar drill hole database consists of 217 diamond drill holes (86,900 m). At the time of writing, Minera Peregrine Argentina S.A. was conducting a metallurgical program, environmental baseline study, and preliminary economic evaluations for a copper-gold mining project at Altar. The ore potential of this region of the San Juan Province (Argentina) is highlighted by the discovery of several porphyry Cu districts, such as Piuquenes, Rincones de Araya, Quebrada de la Mina, Yunque, Los Azules, and Los Bagres Sur (Mpodozis and Cornejo, 2012; Fig. 1A).

The early Miocene lower volcanic complex with U-Pb zircon ages of 21.6 ± 1.2 Ma, 20.8 ± 0.3 Ma (Maydagán et al.,

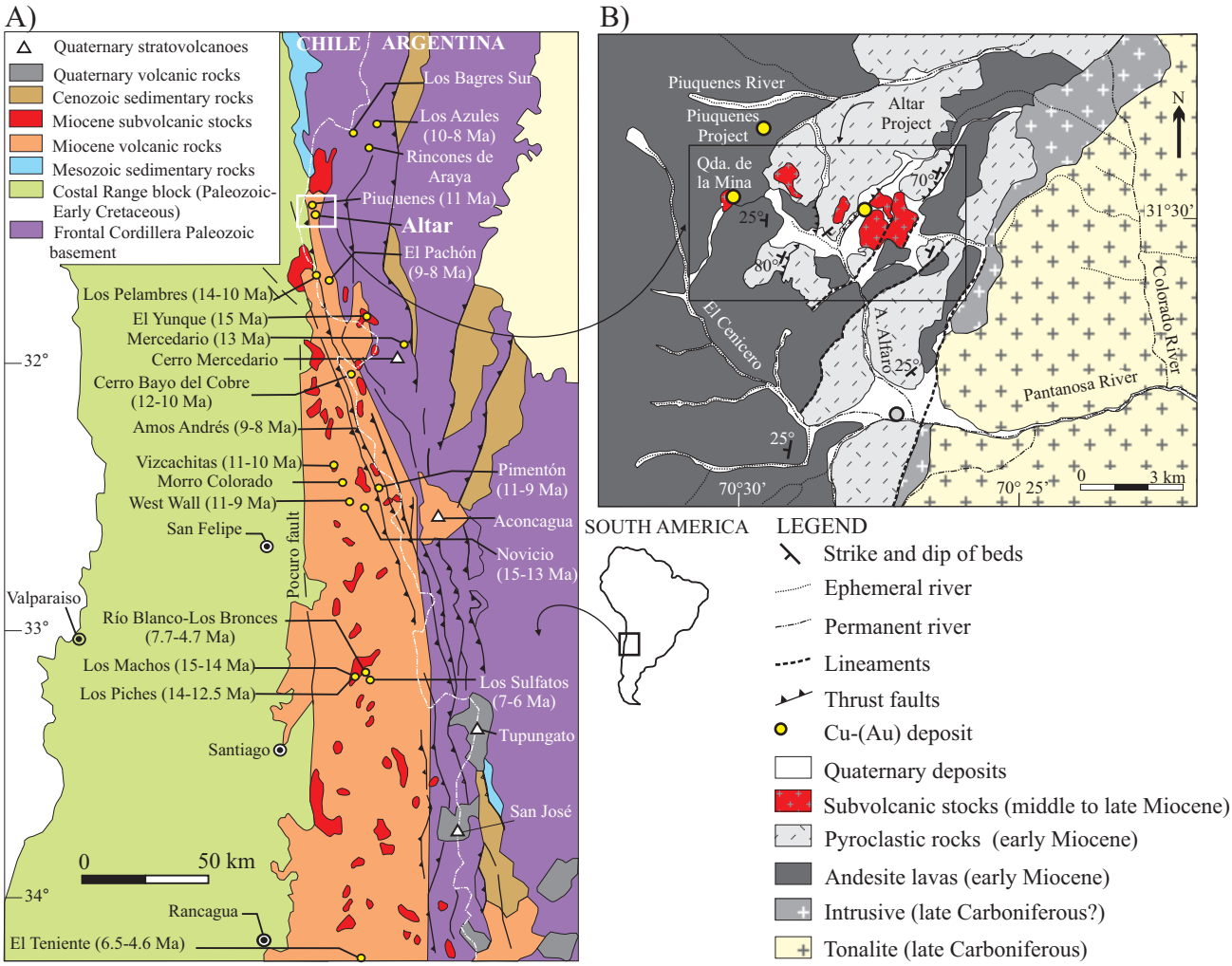

FIG. 1. A) Geologic map of the Abanico intra-arc basin showing the location and ages of the Miocene-Pliocene porphyry copper deposits of Chile and Argentina (Mpodozis and Cornejo, 2012, and references therein). B) Geologic map of Altar project area.

2011, 2014; Maydagán, 2012), and 21.9 ± 0.2 Ma (Gatzoubaros et al., 2014) is composed of intercalations of lava flows and thin pyroclastic units that grade upward into a thick massive tuff. The volcanic rocks are intruded by porphyritic andesite-dacite intrusions and breccias of the middle to late Miocene upper subvolcanic suite (Maydagán et al., 2011, 2014; Fig. 1B). The Altar upper subvolcanic suite comprises a premineralization intrusion (porphyry 1; 11.75 ± 0.24 Ma), three mineralized intrusions (porphyry 2, 11.62 ± 0.21 and 11.68 ± 0.27 Ma; porphyry 3, 11.13 ± 0.26 Ma; porphyry 4, 10.35 ± 0.32 Ma), mineralized breccias (matrix supported and hydrothermal cemented breccias), two postmineralization intrusions (andesite porphyry and porphyry 5), and a late post-mineralization matrix-supported breccia (Late breccia; 8.9 ± 0.4 Ma; Maydagán et al., 2014, Fig. 2A, B). Mineralization in the Altar deposit (995 Mt, 0.35% Cu, 0.083 g/t Au; Marek, 2014) is mainly hosted in a complex stockwork of quartz veinlets and disseminations. The outer limit of alteration and mineralization defines the Altar hydrothermal system to be ~4 × 3 km in surface dimensions (Fig. 3A). The three mineralized intrusions were emplaced within ~0.7 to 1.3 m.y. (Maydagán et al., 2014) and formed two magmatic hydrothermal centers with mineralization located in the east valley (the older) and the central ridge (the younger; Fig. 3B-D).

Distribution of Cu, Au, and Mo mineralization

Metal assays were performed at Acme Analytical Laboratories in Santiago (Chile) at intervals of 2 m (Peregrine Metals Ltd., 2011). Drill hole sample crushing and pulverizing were completed at the Acme sample preparation facility in Mendoza, Argentina. Thirty-three elements were analyzed by ICP-emission spectrometry (ES) using an aqua regia digestion, and Au was analyzed by fire assay with atomic absorption spectrometry (AAS) using a 30-g sample.

The two main Cu centers are spatially associated with porphyries 2 and 4, respectively (Fig. 3B). Another Cu center, with less mineralization, correlates with porphyry 3 in the central ridge. Geochemistry of Cu, Au, and Mo delineates two mineralized centers located in the central ridge (central orebody) and the east valley (east orebody; Fig. 3B, C). Copper-(Au) grades are spatially related with the areas of emplacement of the mineralized intrusions and of vein stockwork that cut

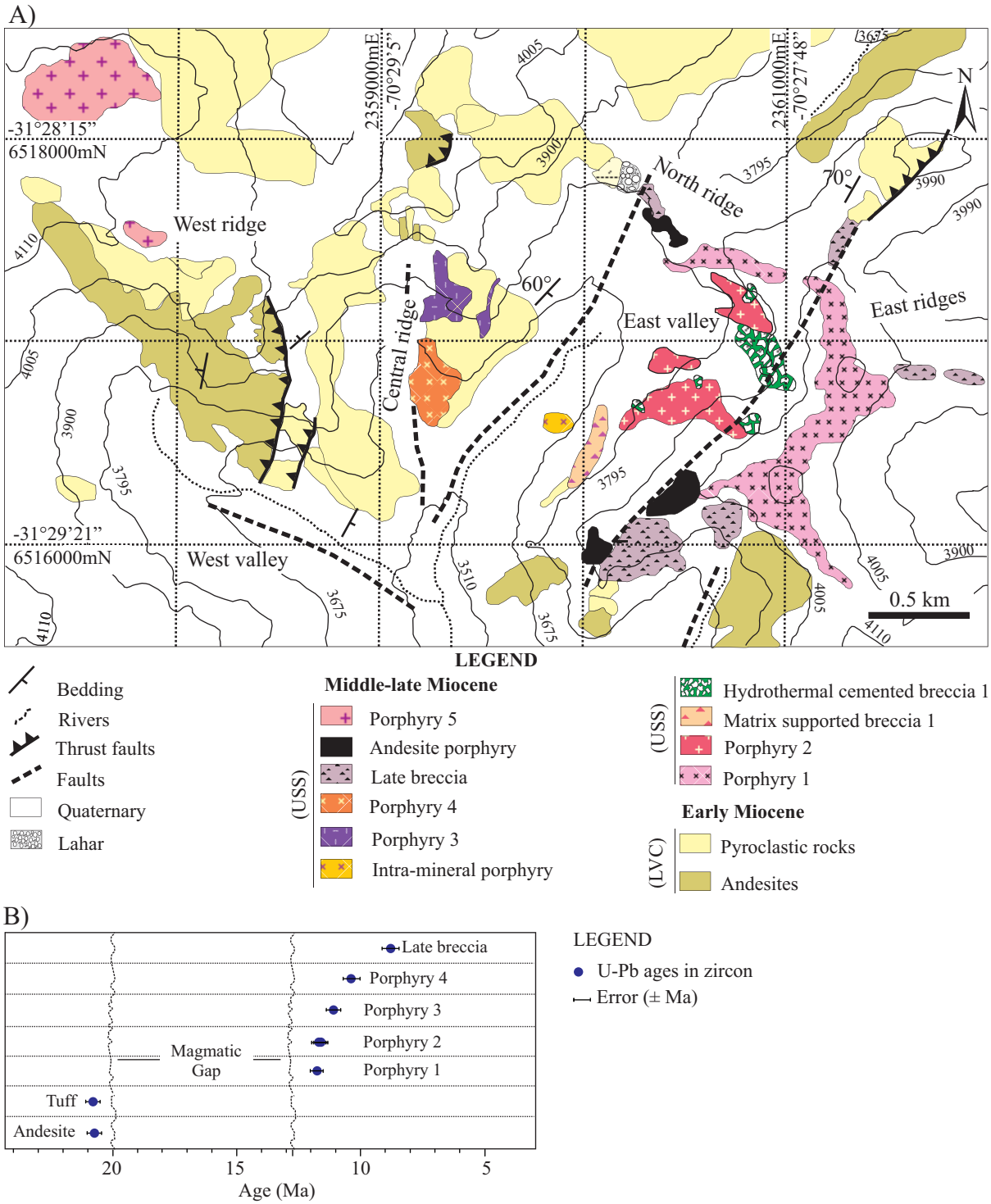

FIG. 2. A) Detailed map of Altar geology. Locations are given in Gauss Krueguer coordinates, Inchauspe (2). B) Summary of U-Pb data of Altar rocks (Maydagán et al., 2011, 2014).

and surround two zones of potassic alteration at depth (Fig. 3B-D).

Gold concentration at Altar is low compared with the Cu-Au-porphyries of the Andean back-arc region, but higher than that observed in the giant Miocene deposits of Chile, with an average Au/Cu ratio of 0.14×10^{-4} by weight across the central orebody (Zwahlen et al., 2014). In the central orebody, Mo mineralization forms an extensive and continuous halo that surrounds porphyry 4 and is more developed in the wall rocks (Fig. 3C, D), whereas in the east orebody, two small occurrences of Mo mineralization can be recognized. The average Mo resource grade obtained in the drill holes

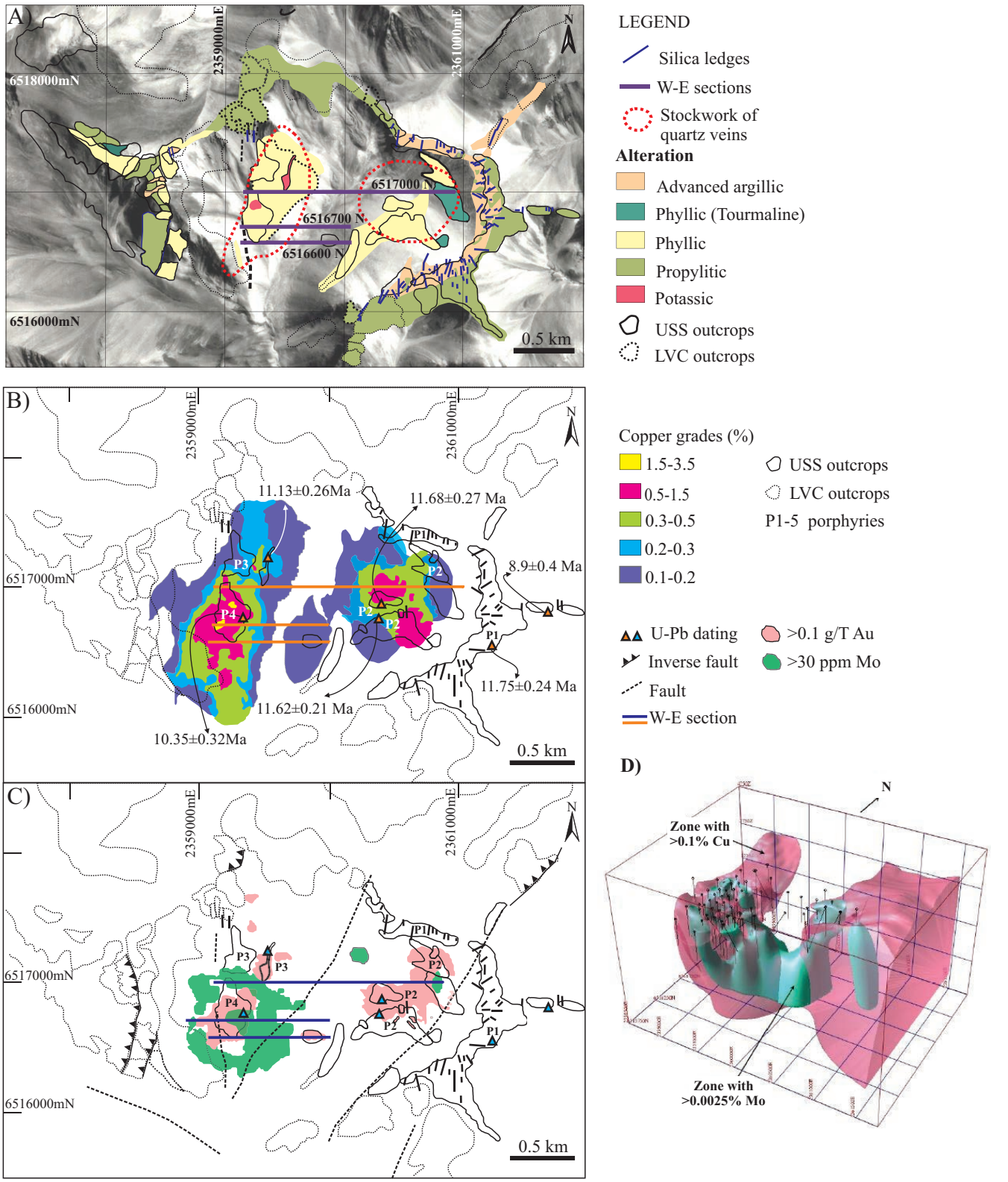

FIG. 3. A) Map with the distribution of hydrothermal alteration and location of the three sections analyzed. B) Cu distribution considering the grades of the drill holes below the leaching zone (Peregrine Metals Ltd., 2011). C) Zones with Mo grades higher than 30 ppm and Au grades higher than 0.1 g/t recognized in the drill holes, extrapolated to the surface (Peregrine Metals Ltd., 2011). D) Three-dimensional model with areas of >0.1% Cu and >0.0025 ppm Mo.

of the project is 0.002%. Epithermal siliceous ledge samples from the eastern ridges of the deposit assay several % copper, >100 g/t Ag, and ~0.5 g/t Au.

Analytical Techniques and Sampling Methodologies

Field data were collected from outcrops and by examination of approximately 10,000 m of core from 25 selected drill holes from three cross sections across the deposit (6717000 N, 6716700 N, and 6716600 N). Over 400 samples representing the different lithologies, alteration zones, and mineralization were analyzed by binocular microscope and by transmitted and reflected light microscopy.

The detailed study of Altar samples allowed identifying types and subtypes of veins (Table 1). Over 200 samples and 44 surface samples were analyzed by X-ray diffraction and infrared spectroscopy (Tables 2, 3).

CL, trace elements, and microthermometry studies were focused on quartz from veins that cut the porphyry 4 of the central orebody (Altar Central), where it was possible to observe the complete sequence of veins of the porphyry deposit. The same methodology was used to study the epithermal siliceous ledges that crop out on the east ridges of the deposit and belong to the east orebody (Altar East). Twenty-one veins, representing all stages of mineralization, were imaged via panchromatic and color scanning electron microscope (SEM)-cathodoluminescence—each accompanied by a backscattered electron (BSE) and secondary electron (SE) image.

LA-ICP-MS semiquantitative line scans of trace elements in quartz were measured using a Resonetics laser M-50-LR, an ArF laser (193 nm) Excimer laser ablation system, coupled to an Agilent 7700x quadrupole ICP-MS at the University of New Brunswick (see McFarlane and Luo, 2012). Line scan analyses have the advantage of showing, more clearly than spots, the correlations among trace element concentrations and between CL textures and trace element distribution (cf. Rusk et al., 2011), whereas spot analyses generally offer both higher precision and higher spatial resolution.

Quantitative quartz trace element analysis was carried out at Western Washington University using a NewWave 213-nm Nd YAG laser coupled to an Agilent 7500ce quadrupole mass spectrometer. Due to the presence of mineral and fluid inclusions, we conservatively present quantitative data for only ^{7}Li, ^{27}Al, ^{49}Ti, and ^{74}Ge (Tables 4, 5). Average detection limits (>99% confidence) of these elements for an 80-μm spot are ~13, ~50, ~150, and ~150 ppb, respectively. We also analyzed numerous other elements including Na, P, K, Ca, Mn, Fe, Cu, Zn, Ga, As, Sr, Mo, Sn, Sb, Ba, and Pb, but due to uncertainties related to abundant fluid and mineral inclusions, we do not present quantitative results for these elements.

Helium was used as the carrier gas and was mixed with Ar prior to entering the torch. An energy density of ~15 to 20 J/cm^2 combined with a laser pulse frequency of 10 Hz resulted in controlled ablation of quartz, producing cylindrical pits with little spalling or catastrophic fracturing of the quartz. The spot size was 80 μm in diameter for all spots. For each analysis, background was collected for ~30 s and the spot was ablated for ~40 to 60 s. Data was reduced with GLITTER using ^{30}Si as an internal standard assuming stoichiometric quartz (Si = 467,434 ppm). Standard reference material NIST 610 was used as an external calibration standard with elemental concentrations of Jochum et al. (2011). Quartz analyses were bracketed by standard analyses and a linear drift correction was applied. ICP-MS signals were closely inspected for the accidental analysis of fluid or mineral inclusions, and where such inclusions were present, they were excluded from the signal integration, or, if this was not possible, the result was discarded.

A total of 191 microthermometric analyses on fluid inclusions in quartz (six samples) and anhydrite (one sample) were performed from selected veins. Analyses were carried out using a Linkam fluid inclusion cooling-heating stage at the Fluid Inclusion Laboratory of the Universidad Nacional del Sur, Bahía Blanca, Argentina, and a Linkam FTIR600 stage at the Centro de Desenvolvimento da Tecnologia Nuclear, Belo Horizonte, Brazil. The analyses were performed on fluid inclusion assemblages, defined as coevally entrapped groups of inclusions characterized by a close spatial association and identical phase proportions at room temperature (Goldstein and Reynolds, 1994; Tables 6, 7). Each fluid inclusion assemblage contains between two and eight individual inclusions.

The Linkam stage has an upper temperature limit of 550°C and was calibrated to ±1.0°C for the critical point of pure H_2O (374.1°C) and ±0.5°C for the melting point of CO_2 (–56.6°C). The volatile components of selected fluid inclusions were analyzed using Raman microspectroscopy at the Departamento de Engenharia, Universidade Federal de Minas Gerais, Belo Horizonte, Brazil. Raman spectra were obtained on a Horiba Jobin Yvon LABRAM-HR 800 spectrograph, equipped with a 633-nm helium-neon laser and 20 mW of power, attached to an Olympus BHX microscope. The spectral resolution was 2 μm and a minimum of 10 scans with 60-s integration times were recorded.

Results

Deposit geology

The three sections presented illustrate the more explored and deeper Cu-(Au-Mo) orebody located in the central ridge of the deposit (Fig. 4). The section located north (6517000 N) intercepts the massive tuff of the lower volcanic complex (Fig. 4A) and the sections located farther south (6516700 and 6516600 N) cut an intercalation of basaltic andesite and andesite-dacite lavas covered by a thick level of massive tuff (Fig. 4B, C). In the east, the sections intercepted the porphyry 2 intruded by the hydrothermal cemented breccia 1 and the matrix-supported breccia 1, and in the central ridge, the porphyries 3 and 4 and the matrix-supported breccia 2 (Fig. 4A, B).

Alteration and mineralization in the porphyry deposit

The mineralized subvolcanic intrusions (porphyries 2, 3, and 4) contain a similar sequence of alteration and mineralization events. Quartz + biotite ± anhydrite ± K-feldspar ± albite ± rutile ± muscovite alteration (potassic alteration) contains very fine grained (<0.4 mm) chalcopyrite (~1–3 vol %) ± pyrite ± molybdenite ± bornite (traces) crystals disseminated and in early veins. Potassic alteration occurs as patches at shallow and intermediate levels affecting the porphyries and the wall rocks and is pervasive at depth (Fig. 4A, B). In section

TABLE 1. Characteristics of the Porphyry Cu (Au-Mo) Altar Veins and Epithermal Siliceous Ledges (in a relative age sequence, older at the top)

		Vein filling						Alteration halo	
		Major		Minor					
Type	Subtype	Gangue	Opaques	Gangue	Opaques	Thickness	Structure	Gangue	Opaques
Type EB[1]		bio + qtz		rt	mt	0.1–1 mm	Capillary veinlets	ksp	None
Type A[2]	A1	qtz		anh ± ksp ± rt		1 mm–4 cm	Irregular to straight walls	ksp ± bio ± rt	None
	A2		cpy	ksp ± qtz ± bio anh ± rt	py	1–3 mm	Capillary veinlets	ksp ± anh	None
Type B[2]		qtz			mo ± cpy ± py ± rt	2 mm–2 cm	Straight to irregular walls	ksp ± bio	None
Type C		chl + hm		rt		0.2–1 mm	Capillary veinlets	None	None
Type D[2]	D1	qtz	py + cpy	ill ± tour ± rt		2 mm	Irregular walls	qtz + ill ± rt ± tour	py ± cpy
	D2	qtz	py	ill ± rt	cpy	1 mm–6 cm	Irregular to straight walls	qtz + ill ± rt ± tour	py
		tour + qtz			py ± cpy	0.5 mm–1 cm	Irregular walls	qtz + ill ± rt	None
Type E[3]	E1		tn ± py	qtz	td, gold (cpy, bn)	0.5 mm–3 cm	Irregular to straight walls	kaol ± qtz ± rt	tn (cpy, bn) + py ± (gold)
	E2		py	qtz			Irregular to straight walls	kaol ± qtz ± rt	py, tn (bn)
	E3		py + en	qtz	(cpy, bn, tn)	2.5 cm	Irregular to straight walls	None; qtz; kaol ± qtz ± rt	py + en
	E4	qtz	py + gn + sl			2–12 cm	Straight walls	None	None
		anh		qtz ± ca		1 cm	Straight walls	None	None
Epithermal		qtz				1–3 m	Straight walls	qtz + alun ± rt, qtz + kaol	None
		qtz + alun ± bar	en			1 mm–1 m	Straight walls		en

Abbreviations: ab = albite, alun = alunite, anh = anhydrite, bar = barite, bio = biotite, bn = bornite, ca = calcite, chl = chlorite, cpy = chalcopyrite, en = enargite, ga = galena, hm = hematite, ill = illite, kaol = kaolinite, ksp = potassium feldspar, mo = molybdenite, ms = muscovite, mt = magnetite, py = pyrite, qtz = quartz, rt = rutile, sl = sphalerite, td = tetrahedrite, tour = tourmaline, tn = tennantite

[1] Gustafson and Quiroga (1995)

[2] Gustafson and Hunt (1975)

[3] Masterman et al. (2005)

Table 2. XRD Analyses of Samples, Sections 65166700 mN and 6517000 mN

Sample no.	Total fraction mineralogy (%) Transparent minerals	Opaque minerals	Fraction <2-μm mineralogy (%) and IK
ALD-1-7		hem, jar	ill, IK: 0.31 (90), chl (10)
ALD-1-58	plag (54), clay (33), gy (3)	py, cpy (hm), dg, cv	chl (80), ill IK 0.21 (20)
ALD-1-86	qtz (55), clay (37), plag (5), anh (3)	jar	ill (100), IK: 0.20
ALD-1-107	qtz (43), clay (49), plag (5), anh (3)	jar	ill (100), IK: 0.38
ALD-1-150	qtz (72), clay (25), anh (3)	jar	ill (100), IK: 0.15
ALD-1-190	plag (64), qtz (17), clay (17), anh (2)	mg	chl (100)
ALD-1-296	qtz (58), clay (37), plag (5)	py, cpy, cv, dg, en	ill, IK: 0.13 (100)
ALD-1-300	qtz (53), clay (41), plag (3), anh (3), py	py, cpy, dg, cv	ill, IK: 0.13 (100)
ALD-1-327	qtz (63), clay (31), plag (6)	cpy, py, dg, cv	ill, IK: 0.15 (100)
ALD-1-340	plag (40), qtz (30), clay (30), anh (t)	cpy, py, (hm), dg, cv	ill, IK: 0.15 (75), chl (25)
ALD-1-353	qtz (56), clay (38), plag (3), anh (3)	cpy, py, cv, dg, en	ill, IK: 0.15, chl (t)
ALD-1-362	plag (45), qtz (33), clay (20), anh (2)	cpy, py, dg, cv	ill, IK: 0.11 (90), chl (10)
ALD-1-375	qtz (64), clay (24), plag (10), anh (2)	cpy, py, dg	ill, IK: 0.13 (94), chl (6)
ALD-1-382	clay (39), qtz (33), plag (15), gy (10), anh (2)	cpy, py, dg	ill, IK: 0.15 (90), chl(10)
ALD-1-406	clay (52), qtz (34), y (10), plag (2), anh (2)	cpy, py, bn, dg, cv	ill, IK: 0.23 (96), chl (4)
ALD-1-414	clay (66), qtz (27), plag (5), anh (2)	py, cpy, tn, en	ill, IK: 0.11 (100)
ALD-1-444	qtz (55), clay (37), plag (4), anh (4),	py, tn, en	ill, IK: 0.12 (100)
ALD-1-456	qtz (58), clay (34), plag (3), gy (3), anh (2)	py, tn, en	ill, IK: 0.13 (100)
ALD-1-466	plag (50), qtz (25), clay (15), gy (8), anh (2)	cpy, py, en	ill, IK: 0.13 (90), chl (10)
ALD-4-33	qtz (45), plag (19), clay (11), anh (1)	hm, jar, py (t)	ill (100)
ALD-4-67	qtz (50), clay (50)	jar	ill (100)
ALD-4-86	qtz (53), clay(45), plag (2)	jar	ill (100)
ALD-4-135	plag(48), qtz (27), clay (25)	jar	chl (100)
ALD-4-148	qtz (35), plag (34), clay (31)	hm	ill (100)
ALD-4-172	qtz(55), y (30), clay (14), plag (1)	cpy, dg, py (t)	ill (100)
ALD-4-299	qtz (43), clay (47), ksp(10)		ill (100)
ALD-4-370	qtz (55), clay (26), plag (15), gy (4)	py	
ALD-4-378	plag (53), clay (21), qtz (19), gy (7)	cpy, py, hm	chl (100)
ALD-4-387	qtz (47), clay (42), y (6), plag (3), ksp (2)	py	
ALD-4-428	plag (35), qtz (27), clay (22), anh (13), gy (3)	py, cpy	ill, chl
ALD-4-436	plag (45), clay (22), qtz (21), anh (10), gy (2)	py, cpy	ill, chl
ALD-4-467	qtz(54), clay (30), plag(6), anh (6), gy(3), ksp (1)	py, cpy	ill (100)
ALD-4-477	plag(44), clay(20), qtz(23), anh (12), gy(1)	py, cpy	ill, chl
ALD-4-479	plag(43), qtz(21), anh(20), clay (16)	py, cpy	ill, chl
ALD-4-489	qtz (49), clay(25), gy (17), plag (6), anh (2)	py, cpy	ill (100)
ALD-4-500	plag (46), qtz (34), clay (10), (5), anh (5)	py, cpy	ill, chl
ALD-43-210	qtz >> clay > plag , ksp , anh , gy (t)	py, cpy, bn, en, dg	ill, chl (t)
ALD-43-229	plag >> clay > qtz , gy (t)	py, cpy, tn, en, dg	ill (46), chl (40), kaol (14)
ALD-43-263	qtz > clay >>plag > ksp, anh , gy (t)	py, cpy, tn, , dg, cv	ill (77), chl (12), kaol (11)
ALD-43-661	qtz > plag >> clay > anh, gy (t)	cpy, py	ill (100)
ALD-43-690	plag > qtz >> clay = anh , gy (t)	hm, bn, tn, dg, cv	ill, chl (t), kaol (t)
ALD-43-745	plag > qtz >> clay = anh , gy (t)	cpy, py	ill (100)
ALD-43-869	plag > qtz >> clay = anh , gy (t)	cpy, py, tn (t)	ill, kaol (t)
ALD-43-907	plag > qtz >> clay = anh, gy (t)	cpy, py, hm	ill, kaol (t), chl (t)

Analysis performed with X-ray diffractometer and polarizing microscope; numbers in parentheses indicate the proportion determined by methods of quantification

Abbreviations: anh = anhydrite, bn = bornite, chl = chlorite, clay = clay + mica, cpy = chalcopyrite, cv = covellite, dg = digenite, en = enargite, gy = gypsum, hm = hematite, IK = Kubler index, ill = illite, jar = jarosite, kaol = kaolinite, ksp = K-feldspar, mo = molybdenite, plag = plagioclase, py = pyrite, qtz = quartz, t = traces, tn = tennantite

6516700 N, in deep sectors of the porphyry 4 (Fig. 4B), hydrothermal albite (>30 vol %) contemporaneous with the potassic alteration obliterated the original porphyritic texture of the rock and gave it a granular appearance. The assemblage chlorite + quartz + muscovite ± rutile and illite (chloritic alteration) is found in patches at deep, intermediate, and shallow levels (Fig. 4). The mineralization in this alteration consists of hematite (0.5–2 vol %, >0.7 mm) plus chalcopyrite (~ 2 vol %, 0.1–0.5 mm) + pyrite (<1.5 vol %, 0, 5 mm) ± bornite (trace) that are preserved from the previous potassic stage.

The assemblage quartz + muscovite ± tourmaline ± rutile and illite (phyllic alteration) affects all lithologies. It forms a continuous halo surrounding the potassic core and the chloritic alteration patches (Fig. 4). At depth it is controlled by fractures and forms the halos of D veins (Table 1). The rock fragments and the matrix of the breccias of the east valley and central ridge are ubiquitously affected by phyllic alteration. The mineralization consists of pyrite ± chalcopyrite as part of a stockwork of D veins and veinlets and as very fine grained (<1.2–<0.8 mm) disseminations (0.2–7 vol %) in the altered rocks.

The assemblage kaolinite (differentiated by infrared spectroscopy) ± quartz ± rutile (weak advanced argillic alteration) at depth is localized in fractures that cut the porphyritic intrusions and the wall rocks. It is poorly developed and generally overlaps zones with phyllic alteration, although it has been recognized cutting potassic alteration zones (Fig. 4B, C). This alteration type forms the halos of east veins (Table 1). The

TABLE 3. XRD Analysis of Samples from Section 6516700 mN

Sample no.	Total fraction mineralogy opaque minerals	Fraction <2-μm mineralogy (%) and IK
ALD-57-79,3	gold (t)	ill (100)
ALD-57-223	py, en, tn, dg	ill (100)
ALD-57-317	cpy, py	ill, kaol (t)
ALD-57- 317	hm	ill, kaol (t)
ALD-57 -338	cpy, py	ill (100)
ALD-57- 366	cpy, py	ill (40), kaol (40), chl (20)
ALD-57-374	cpy, py	ill (100)
ALD-57- 374	cpy, py	ill, kaol (t)
ALD-57- 434	hm	ill (100)
ALD-57-622	cpy, py	ill (100)
ALD-57-672	cpy, py, tn	ill (100)
ALD-49- 77	py	ill (54), chl (35), kaol (11)
ALD-49- 142	cpy, py, dg, cv	ill (50), chl (38), kaol (12)
ALD-49- 161	dg	ill (100)
ALD-49- 170	dg + cv	ill (40), chl (30), kaol (30)
ALD-49- 192	py	ill (100)
ALD-49- 289	py + cpy, tn	ill (100)
ALD-49- 483	cpy, py	ill (100)
ALD-49- 498	tn	ill (100)
ALD-49- 553	cpy, py	ill (100)
ALD-49- 611	cpy, py, bn, en, tn	ill (64), chl (21), kaol (15)
ALD-46- 67	hm	ill (100)
ALD-46- 89	cpy, py, dg, cv	ill (100)
ALD-46- 107	cpy, tn, dg, cv	ill (100)
ALD-46- 246	cpy, py, bn	ill, kaol (t), chl (t)
ALD-46- 261	cpy, py, bn, hm	ill, kaol (t), chl (t)
ALD-46- 271	cpy, py	ill, kaol (t), chl (t)
ALD-46- 321	cpy, py, en, cv	ill (60), kaol (30), chl (10)
ALD-46- 434	cpy, py	ill (100)
ALD-46- 496	cpy, py	ill (100)
ALD-46- 540	tn, py, gold (t)	kaol (56), ill (38), chl (6)
ALD-46- 593	cpy, py, tn, bn	ill (100)
ALD-14-42	hm	ill (53), kaol (32), chl (15)
ALD-14-182.9	cpy, py	ill (100)
ALD-14-317	cpy, tn, dg, cv, hm	ill (64), chl (20), kaol (16)
ALD-14-353	cpy, py	ill (100)

Analysis performed with X-ray diffractometer and polarizing microscope; numbers in parentheses indicate the proportion determined by methods of quantification

Abbreviations: bn = bornite, chl = chlorite, cpy = chalcopyrite, cv = covellite, dg = digenite, en = enargite, hm = hematite, IK = Kubler index, ill = illite, kaol = kaolinite, py = pyrite, t = traces, tn = tennantite

quartz in equilibrium with this alteration commonly contains gold grains (10–20 μm). Mineralization associated with this alteration consists of pyrite, tennantite, bornite, enargite, tetrahedrite, and gold.

Supergene alteration resulted in a zone of leaching and a zone of sulfide enrichment at depth. The leaching area has a thickness between 30 and 310 m (Fig. 4). In contact with the leaching zone, there is a supergene enrichment zone with a thickness of 100 to 250 m. This area contains digenite ± covellite replacing chalcopyrite, bornite, and tennantite. In the porphyries, this zone shows higher Cu values (up to 3.5% Cu), which decrease toward the wall rocks (up to 1.5% Cu).

Altar drill holes, with lengths between 300 and 1,000 m, allowed us to examine the extensive record of veining, their variations with depth, and relationship to disseminated mineralization and alteration envelopes. The detailed study of Altar samples permitted the definition of six types of veins (see Gustafson and Hunt, 1975; Gustafson and Quiroga, 1995; Masterman et al., 2005) and their subtypes (Table 1).

Quartz + biotite + rutile ± magnetite veinlets (type EB): These are the oldest veinlets; they are thin (<1 mm) and have irregular walls (Table 1, Fig. 5A). EB veins are similar to early dark micaceous (EDM) veins from Butte, Montana, as described by Meyer et al. (1968). Where these veinlets cut plagioclase phenocrysts, they commonly have a halo of secondary K-feldspar. Sulfides (chalcopyrite ± pyrite) are present only where other mineralized veins cut the rock. They are generally found in deep areas with potassic alteration where they cut the porphyries and the andesite of the lower volcanic complex. In zones with chloritic alteration, EB veinlets are altered to chlorite + rutile ± hematite, chalcopyrite ± pyrite (C veins, Table 1) and are commonly cut by A2 veinlets (see below), generating false reverse cutting relationships.

Quartz ± potassium feldspar ± chalcopyrite ± pyrite ± rutile veinlets (type A): These veins have wavy to straight walls and thicknesses ranging from ~1 mm to 4 cm (Fig. 5B). They have a granular internal texture with no internal symmetry. Anhedral quartz grains (0.1–0.8 mm) occupy 90 vol % of subtype A1 veins. Rutile crystals (<1 mm) occur within the quartz and in the halos of the veins. Very wormy and wispy examples of these veins have been identified in the deepest levels reached by drilling (e.g., between 651 and 869 m of ALD-43). Veins with very irregular walls are old and are cut by younger and thin veins with straight walls. At intermediate and shallow levels, A1 veins have straight walls. Where these veins cut the andesite of the lower volcanic complex, they have a halo of potassium feldspar + biotite ± rutile (Fig. 5B). A1 veins cut type EB veinlets in the porphyries with potassic alteration (Fig. 5A). They cut the porphyry 2 and the wall rocks in the east orebody and porphyries 3 and 4 and the wall rocks in the central orebody (Fig. 6). Subtype A2 veins consist of chalcopyrite ± quartz ± feldspar ± biotite ± anhydrite ± pyrite ± rutile (Table 1) and are thin (<3 mm) veinlets and seams that cut A1 (Fig. 5C). In contact with wall-rock plagioclase, they have a very thin halo of secondary K-feldspar (Fig. 5C). They are located at deep levels in porphyries 2, 3, and 4, and in wall rocks with potassic alteration contiguous with the porphyritic intrusions (Fig. 6).

Quartz ± molybdenite ± pyrite ± chalcopyrite ± rutile veinlets (type B): These are characterized by abundant quartz with subordinate amounts of sulfides and rutile (Table 1). They range from a few millimeters to ~2 cm in thickness and have straight walls (Fig. 5D). Molybdenite crystals generally occur as thin platy crystals on the margin of the veins. Chalcopyrite and pyrite (0.1–0.2 mm) are interstitial between quartz grains and accompany the molybdenite in subordinate amounts (Fig. 5E). B veins are generally associated with phyllic altered rocks, because they are commonly reopened and filled by pyrite + chalcopyrite microveinlets and late anhydrite and calcite. They cut A veins and potassic alteration zones (Fig. 5F). They are abundant in the central orebody, where they cut the porphyry 4 and wall rocks at intermediate to deep levels, and occur in the east orebody with a lesser intensity cutting the porphyry 2 at intermediate depths (Fig. 6).

Quartz + pyrite ± chalcopyrite ± tourmaline ± rutile veinlets (type D): These veins are characterized by phyllic alteration halos that range from 0.1 to 2 cm (Table 1). Their halos are typically depleted in sulfides (pyrite and chalcopyrite) relative to the previously mineralized rock. Two subtypes of

TABLE 4. Trace Elements in the Quartz of A and B Veins Analyzed with LA-ICP-MS

Vein type and notes	Sample no.	^{7}Li (ppm)	^{23}Na (ppm)	^{27}Al (ppm)	^{39}K (ppm)	^{49}Ti (ppm)	^{72}Ge (ppm)	^{75}As (ppm)	^{118}Sn (ppm)	^{121}Sb (ppm)
A2 vein	ALD-43-745	2.6	18	66	5.5	96	0.5	0.4	0.1	<0.01
CL-bright quartz	ALD-43-745	2.4	38	448	132	74	0.4	0.7	0.3	0.1
	ALD-43-745	3.0	185	222	127	125	0.6	0.5	0.2	<0.02
	ALD-43-745	2.9	15	82	1.9	77	0.5	0.2	0.0	0.0
	ALD-43-745	3.0	179	330	161	93	0.5	0.6	0.1	0.0
	ALD-43-745	3.9	184	280	116	115	1.2	0.7	0.4	0.1
	ALD-43-745	2.8	164	138	24	94	1.5	0.5	0.5	<0.03
	ALD-43-745	2.7	92	100	13	107	1.1	0.7	0.3	0.0
	ALD-43-745	2.5	365	199	159	141	0.7	0.1	0.3	<0.02
	ALD-43-745	2.0	393	142	114	93	0.4	0.4	0.2	<0.02
	ALD-43-745	2.8	200	96	240	111	0.9	0.3	0.5	0.0
	ALD-43-745	2.9	25	244	72	106	0.8	<0.09	0.1	<0.01
	ALD-43-745	2.5	526	153	493	138	0.8	1.0	0.3	0.0
	ALD-43-745	1.9	180	65	113	75	1.4	1.2	0.1	0.0
	ALD-43-745	2.1	499	213	212	76	1.2	1.4	0.2	0.0
	ALD-43-745	2.5	119	179	62	107	0.7	0.2	0.2	0.0
	ALD-43-745	2.9	36	378	110	137	0.9	0.3	0.2	<0.01
	ALD-43-745	3.6	93	421	145	75	0.9	0.2	0.1	<0.008
	ALD-43-745	2.4	355	169	149	108	0.7	0.5	0.2	0.0
	ALD-43-745	2.2	104	322	121	130	0.5	0.2	0.2	<0.02
	ALD-43-745	2.4	372	196	54	128	0.6	0.1	0.1	0.0
	ALD-43-745	2.2	118	242	124	140	0.5	0.1	0.1	<0.02
	Min	1.9	15	65	1.9	74	0.4	0.1	0.0	0.0
	Max	3.9	526	448	493	141	1.5	1.4	0.5	0.1
	Average	2.6	194	213	125	107	0.8	0.5	0.2	0.0
A2 vein	ALD-16-141	2.0	720	137	190	76	0.6	0.5	0.2	0.0
CL-bright quartz	ALD-16-141	2.4	284	204	111	145	0.9	<0.13	0.1	<0.02
	ALD-16-141	3.1	942	191	450	81	1.8	1.7	0.4	<0.01
	ALD-16-141	2.4	574	117	226	83	1.1	0.6	0.3	<0.01
	ALD-16-141	2.0	609	131	83	78	0.8	0.4	0.1	<0.02
	ALD-16-141	2.4	274	91	131	76	1.4	0.6	0.2	0.0
	ALD-16-141	2.3	326	129	198	102	0.9	0.4	0.2	<0.01
	ALD-16-141	2.9	977	132	447	116	0.7	0.4	0.2	<0.01
	ALD-16-141	2.4	282	127	100	125	0.4	<0.07	0.2	<0.01
	ALD-16-141	2.4	340	127	126	86	1.2	0.3	0.2	<0.01
	Min	2.0	274	91	83	76	0.4	0.3	0.1	0.0
	Max	3.1	977	204	450	145	1.8	1.7	0.4	0.0
	Average	2.4	533	139	206	97	1.0	0.6	0.2	0.0
A2 vein	ALD-46-271	3.4	42	66	20	94	0.9	0.2	0.4	<0.008
CL-bright quartz	ALD-46-271	3.6	35	83	25	112	0.8	0.5	0.4	0.0
	ALD-46-271	3.9	23	83	13	155	0.6	0.4	0.3	<0.009
	ALD-46-271	3.5	18	68	8	117	0.7	0.1	0.3	<0.008
	ALD-46-271	3.8	137	80	18	134	0.6	1.2	0.3	0.0
	ALD-46-271	3.6	69	98	38	110	0.6	0.6	0.3	<0.01
	ALD-46-271	3.7	21	65	17	95	0.7	0.1	0.3	<0.009
	Min	3.4	18	65	8.2	94	0.6	0.1	0.3	0.0
	Max	3.9	137	98	38	155	0.9	1.2	0.4	0.0
	Average	3.6	49	77	20	117	0.7	0.4	0.3	0.0
A vein reopened by	ALD-55-635	5.5	25	129	<2.13	113	1.1	<0.37	0.1	0.1
B vein	ALD-55-635	7.7	38	142	2.1	114	0.8	0.9	0.2	<0.02
CL-bright quartz	ALD-55-635	7.4	48	132	6.1	110	0.6	0.4	0.1	0.1
	ALD-55-635	12.0	27	236	21	159	1.1	0.6	0.2	0.0
	ALD-55-635	13.2	8	211	4.3	91	1.2	0.3	0.1	<0.02
	ALD-55-635	15.6	4.7	271	13	66	1.6	<0.25	0.1	0.1
	ALD-55-635	10.2	8.5	217	6.6	84	0.9	<0.26	0.1	0.0
	ALD-55-635	12.6	166	278	82	106	1.0	0.9	0.1	0.0
	ALD-55-635	10.2	7.9	197	7.0	93	0.9	0.3	0.1	0.0
	ALD-55-635	9.4	8.6	180	3.6	76	1.1	0.3	0.1	<0.01
	ALD-55-635	11.0	5.1	218	6.0	75	1.0	0.3	0.1	<0.01
	Min	5.5	4.7	129	2.1	66	0.6	0.3	0.1	0.0
	Max	15.6	166	278	82	159	1.6	0.9	0.2	0.1
	Average	10.4	32	201	15	99	1.0	0.5	0.1	0.0

TABLE 4. *(Cont.)*

Vein type and notes	Sample no.	^{7}Li (ppm)	^{23}Na (ppm)	^{27}Al (ppm)	^{39}K (ppm)	^{49}Ti (ppm)	^{72}Ge (ppm)	^{75}As (ppm)	^{118}Sn (ppm)	^{121}Sb (ppm)
A2 vein	ALD-16-141	1.9	215	100	41	15	1.1	0.4	0.1	0.0
CL-dark quartz	ALD-16-141	2.8	119	182	68	23	1.3	0.2	0.1	<0.02
	ALD-16-141	2.6	980	120	480	20	1.6	1.5	0.1	<0.02
	ALD-16-141	2.8	542	127	205	22	1.4	0.5	0.3	<0.02
	ALD-16-141	1.7	246	101	58	15	1.3	1.0	0.2	0.0
	ALD-16-141	1.3	530	96	175	28	1.5	0.6	0.2	<0.01
	Min	1.3	119	96	41	15	1.1	0.2	0.1	0.0
	Max	2.8	980	182	480	28	1.6	1.5	0.3	0.0
	Average	2.2	439	121	171	21	1.4	0.7	0.2	0.0
B vein	ALD-57-551	5.7	8.7	146	2.8	20	0.6	0.3	0.1	0.1
CL-intermediate	ALD-57-551	5.0	45	121	11	25	0.9	0.5	0.1	0.1
quartz	ALD-57-551	2.1	17	76	<2.61	19	1.1	<0.35	0.2	<0.02
	ALD-57-551	4.4	5.1	97	21	17	1.2	0.3	0.1	0.0
	ALD-57-551	5.5	6.5	105	3.1	27	0.9	0.3	0.2	0.0
	ALD-57-551	6.7	88	144	35	24	1.1	<0.39	0.1	0.1
	ALD-57-551	6.2	30	142	25	23	1.1	0.4	0.1	<0.02
	ALD-57-551	4.8	44	102	19	16	1.4	1.0	0.3	0.6
	ALD-57-551	4.7	193	104	61	19	1.0	1.0	0.1	0.1
	ALD-57-551	3.7	183	104	117	21	0.8	0.5	0.1	0.1
	Min	2.1	5.1	76	2.8	16	0.6	0.3	0.1	0.0
	Max	6.7	193	146	117	27	1.4	1.0	0.3	0.6
	Average	4.9	62	114	33	21	1.0	0.5	0.1	0.1
B vein	ALD-43-788	3.3	238	86	93	28	1.1	0.3	0.2	<0.02
CL-intermediate	ALD-43-788	3.9	114	100	39	9.4	4.2	0.6	0.1	0.2
quartz overprinted by	ALD-43-788	2.6	<4.10	84	<2.13	7.1	3.0	<0.245	0.1	0.1
CL-dark quartz	ALD-43-788	6.7	30	230	20	10	2.9	0.8	0.1	0.1
	ALD-43-788	11.3	166	257	99	16	4.1	1.9	0.1	0.2
	ALD-43-788	1.9	<3.60	45	<1.88	19	1.8	0.2	0.1	<0.02
	ALD-43-788	4.8	<3.93	132	<2.06	7.2	2.9	<0.33	0.0	<0.02
	ALD-43-788	2.1	6.5	60	20	10	1.4	<0.30	0.1	<0.02
	ALD-43-788	5.1	8.0	263	5.5	11	2.5	0.8	0.1	0.1
	Min	1.9	6.5	45	5.5	7.1	1.1	0.2	0.0	0.1
	Max	11	238	263	99	28	4.2	1.9	0.2	0.2
	Average	4.6	94	140	46	13	2.7	0.8	0.1	0.1

D veins were recognized: D1 and D2. D1 veins consisting of quartz + pyrite + chalcopyrite ± illite ± tourmaline ± rutile (Table 1; Fig. 7A) have a thickness up to 2 mm. They cut porphyries 2 and 4 at deep to intermediate levels of the sections and, to a lesser extent, they cut the volcanic rocks of the lower volcanic complex. D2 veins consist of pyrite + quartz ± chalcopyrite ± illite ± rutile (0.1–6 cm thick) and have straight walls (Table 1; Fig. 7B). Subhedral pyrite (0.4–3 mm) is the most abundant mineral accompanied by white quartz grains. They contain subordinate chalcopyrite and less illite. Where these veins cut the andesite wall rock, the halos are zoned with an inner phyllic zone without sulfides passing to an outer chloritic zone with disseminated sulfides (pyrite and chalcopyrite). They cut A1 and B veins in deep to shallow levels of the porphyritic intrusions and the wall rocks (see Fig. 7C). No relationship was recognized with D1 veinlets, so they may be transitional. D2 veins are commonly reopened by late anhydrite ± quartz ± calcite veins.

Another variety of veins associated with the phyllic alteration is irregular and thin (0.1–1.5 cm) veinlets composed of radial aggregates (1–4 mm) of acicular tourmaline and a lesser amount of subhedral, fine-grained (<0.2 mm) quartz, pyrite, and chalcopyrite crystals (Table 1). They cut the porphyries, the polymictic matrix-supported breccia 1, and the wall rocks at intermediate and shallow levels, even in areas of leaching. In all these areas they cut A1, D1, and D2 veins (Fig. 8).

Late veins and veinlets rich in sulfides and sulfosalts (type E): They have irregular halos of kaolinite ± quartz ± rutile, and four subtypes have been distinguished: E1, E2, E3, and E4 (Table 1). E1 veins of tennantite (chalcopyrite, bornite) ± quartz ± pyrite ± gold ± tetrahedrite (Table 1) are generally thin (0.5–1 mm) and irregular, but examples up to 3 cm thick at shallow levels are recognized in drill hole A-53 (Fig. 9A). The tennantite replaces chalcopyrite and bornite and is intergrown with fine-grained anhedral pyrite. They generally have subhedral quartz crystals (<5 vol % of the vein) with inclusions of gold (0.05 mm). In the east orebody, E1 veins cut the tuff close to porphyry 2 (Fig. 8). They are most abundant in the central orebody located at intermediate and deep levels, with examples of this vein at depth (ALD-43) cutting porphyry 4 (Fig. 8). E2 veins of pyrite ± quartz (Table 1) have straight walls of varying thickness (Fig. 9B). They have weak advanced argillic alteration (kaolinite ± quartz ± rutile) halos or silicified dark halos due to the presence of small disseminated crystals

TABLE 5. Trace Elements in the Quartz of C, D, E, and Epithermal Veins Analyzed with LA-ICP-MS

Vein type and notes	Sample no.	^{7}Li (ppm)	^{23}Na (ppm)	^{27}Al (ppm)	^{39}K (ppm)	^{49}Ti (ppm)	^{72}Ge (ppm)	^{75}As (ppm)	^{118}Sn (ppm)	^{121}Sb (ppm)
C vein	ALD-55-544	4.0	514	181	66	15	1.1	3.0	0.2	0.1
CL-intermediate	ALD-55-544	6.2	94	337	62	24	1.3	0.7	0.1	0.0
quartz	ALD-55-544	5.4	390	305	55	17	2.1	2.1	0.9	<0.01
	ALD-55-544	7.8	17	260	32	17	0.8	0.3	2.6	<0.02
	ALD-55-544	7.5	47	282	67	16	1.3	0.3	0.4	0.1
	ALD-55-544	10.9	63	163	32	27	1.0	<0.15	0.2	0.1
	ALD-55-544	6.0	228	382	37	26	0.8	<0.10	0.1	<0.01
	ALD-55-544	4.9	185	97	15	19	1.5	1.9	0.7	<0.03
	ALD-55-544	2.0	37	246	30	11	1.5	0.7	2.3	<0.03
	ALD-55-544	1.9	24	40	10	9.1	0.8	0.3	0.9	0.0
	ALD-55-544	5.6	102	92	14	9.1	0.9	0.8	0.2	0.0
	Min	1.9	17.0	40.4	10.1	9.1	0.8	0.3	0.1	0.0
	Max	11	514	382	67	27	2.1	3.0	2.6	0.1
	Average	5.7	154	217	38	17	1.2	1.1	0.8	0.1
D2 vein	ALD-46-496	13	128	470	76	4.6	4.0	10.1	0.5	1.9
CL-dark quartz	ALD-46-496	18	122	557	137	6.6	4.3	8.1	0.6	1.0
	ALD-46-496	15	73	565	233	6.9	2.3	4.8	0.6	0.3
	ALD-46-496	5.9	88	116	41	7.4	2.8	5.6	0.5	0.3
	ALD-46-496	14	258	315	85	7.4	2.6	6.6	0.9	0.6
	ALD-46-496	8.7	92	286	60	7.7	2.5	6.6	0.6	0.5
	ALD-46-496	15	88	368	72	8.0	3.1	8.8	0.9	0.7
	ALD-46-496	13	156	313	91	8.2	3.3	12.7	0.7	1.1
	ALD-46-496	13	211	463	83	8.9	4.2	19.2	0.5	2.0
	ALD-46-496	16	154	834	314	9.2	3.6	11.7	0.6	1.1
	ALD-46-496	12	141	369	77	10	3.8	12.9	0.6	1.4
	ALD-46-496	14	135	753	363	11	3.4	8.3	0.6	0.8
	ALD-46-496	22	225	1,155	384	11	4.8	14.1	0.6	2.1
	ALD-46-496	14	531	833	139	11	4.6	24.2	0.4	3.1
	ALD-46-496	16	280	758	101	13	4.3	17.5	0.4	1.9
	ALD-46-496	20	136	784	93	15	4.7	14.8	0.3	2.1
	ALD-46-496	29	808	1,672	151	16	5.6	16.0	0.6	2.3
	ALD-46-496	23	226	1,401	202	18	4.9	13.4	0.4	1.5
	ALD-46-496	22	608	1,559	154	19	7.7	28.1	0.2	2.8
	Min	5.9	73	116	41	4.6	2.3	4.8	0.2	0.3
	Max	29	808	1,672	384	19	7.7	28.1	0.9	3.1
	Average	16	235	714	150	10	4.0	12.8	0.6	1.5
D2 vein	ALD-46-271	6.1	152	1,174	165	5.5	4.6	30.0	0.4	8.9
CL-dark quartz	ALD-46-271	4.1	99	499	85	4.8	2.7	25.2	0.5	2.1
overprinted by	ALD-46-271	8.6	151	1,434	262	6.8	5.1	28.2	0.5	7.1
late anhydrite +	ALD-46-271	6.1	127	769	126	4.2	4.6	29.4	0.6	3.9
quartz vein	ALD-46-271	9.8	181	1,652	193	5.9	9.6	53.0	0.4	19.6
	ALD-46-271	4.1	120	452	62	4.4	4.6	26.1	0.3	2.2
	ALD-46-271	5.0	390	285	123	4.2	4.4	23.8	0.5	1.2
	ALD-46-271	8.7	170	1,672	58	8	9.3	50.5	0.5	18.9
	ALD-46-271	5.6	146	1,198	199	6.2	7.4	46.4	0.5	12.9
	ALD-46-271	9.2	202	1,744	180	7.0	9.3	47.4	0.6	16.2
	Min	4.1	99	285	58	4.2	2.7	23.8	0.3	1.2
	Max	9.8	390	1,744	262	8	9.6	53.0	0.6	19.6
	Average	6.7	174	1,088	145	5.7	6.2	36.0	0.5	9.3
E4 vein	ALD-4-446	91	176	1,111	302	10	4.4	37.3	0.3	30.5
CL-dark quartz	ALD-4-446	24	79	924	109	0.1	3.4	37.6	0.1	41.5
	ALD-4-446	9.4	16	254	19	0.2	2.3	14.5	0.1	14.2
	ALD-4-446	56	145	1,029	175	2.0	5.6	62.3	0.4	55.0
	ALD-4-446	81	185	870	258	2.0	3.8	32.5	0.2	19.3
	ALD-4-446	46	274	1,519	361	3.2	2.9	14.5	0.1	9.0
	ALD-4-446	197	168	1,235	57	3.2	5.6	29.4	<0.01	77.4
	ALD-4-446	107	250	1,479	296	3.4	8.0	177.0	0.1	79.5
	ALD-4-446	125	106	1,546	103	4.1	7.7	75.3	0.1	65.4
	ALD-4-446	214	69	1,519	47	4.3	9.7	45.3	0.1	32.9
	ALD-4-446	46	179	2,487	679	4.4	2.8	16.0	0.2	9.0
	ALD-4-446	122	275	1,878	480	4.5	4.5	42.0	0.1	31.4
	ALD-4-446	109	266	2,000	422	4.9	5.3	65.7	0.1	49.3
	ALD-4-446	148	117	1,365	134	5.2	8.2	101.7	0.2	116.0

TABLE 5. *(Cont.)*

Vein type and notes	Sample no.	^{7}Li (ppm)	^{23}Na (ppm)	^{27}Al (ppm)	^{39}K (ppm)	^{49}Ti (ppm)	^{72}Ge (ppm)	^{75}As (ppm)	^{118}Sn (ppm)	^{121}Sb (ppm)
	ALD-4-446	13	60	304	51	7.1	9.4	56.3	0.2	83.1
	ALD-4-446	201	97	1,580	121	7.7	8.1	47.8	0.3	41.5
	ALD-4-446	96	372	1,240	446	8.0	4.3	47.7	0.5	22.8
	ALD-4-446	102	106	1,469	148	11	6.5	46.8	0.1	48.4
	ALD-4-446	177	80	1,581	38	14	9.5	35.4	0.1	27.9
	Min	9.4	16	254	19	0.1	2.3	14.5	0.1	9.0
	Max	214	372	2,487	679	14	9.7	177.0	0.5	116.0
	Average	103	159	1,336	223	5.2	5.9	51.8	0.2	44.9
Epithermal vein	ALD-102	23	139	1,326	32	5.5	4.0	67.3	0.1	13.5
at the surface	ALD-102	9.5	49	1,277	93	2.4	3.6	72.3	0.3	45.7
CL-dark quartz	ALD-102	12.2	77	1,023	19	2.5	4.2	102.6	0.4	15.5
	ALD-102	19.8	46	1,272	50	3.0	3.6	74.6	0.3	50.5
	ALD-102	14.8	134	1,324	38	3.1	4.4	115.3	1.1	19.2
	ALD-102	4.6	82	644	15	3.2	4.6	3,271.1	3.7	32.1
	ALD-102	8.4	85	867	42	3.3	3.2	62.7	0.4	54.0
	ALD-102	21.1	593	1,577	77	3.5	5.1	76.6	0.3	38.3
	ALD-102	15.0	304	1,658	83	3.7	4.9	54.7	0.1	10.8
	ALD-102	12.5	263	1,379	38	3.8	4.0	38.8	0.2	10.5
	ALD-102	8.6	308	890	47	3.9	5.4	51.9	0.2	9.8
	ALD-102	18.9	53	1,291	27	3.9	3.9	85.4	0.3	30.9
	ALD-102	8.8	167	653	52	4.0	3.6	206.5	0.1	28.9
	ALD-102	11.6	81	1,097	46	4.3	7.5	54.2	0.2	11.7
	ALD-102	26.5	177	1,765	82	4.7	7.9	80.9	0.1	24.3
	ALD-102	6.1	151	665	21	4.7	4.5	49.8	<0.07	11.8
	ALD-102	24.7	67	1,448	45	5.0	8.4	79.6	0.2	47.1
	ALD-102	19	245	1,338	34	5.5	4.6	71.8	<0.06	13.4
	ALD-102	18.8	110	1,305	43	7.4	6.7	132.0	0.3	76.2
	Min	4.6	46	644	15	2.4	3.2	38.8	0.1	9.8
	Max	26.5	593	1,765	93	7.4	8.4	3,271.1	3.7	76.2
	Average	14.9	165	1,200	47	4.1	5.0	249.9	0.5	28.6

of pyrite (Fig. 9B). At depth, the halos of E1 and E2 veins have disseminated pyrite (0.02–0.8 mm) + tennantite (0.2–0.6 mm) ± trace of tetrahedrite. E2 veins are recognized at intermediate depths cutting porphyry 4 (Fig. 8), porphyry 3, and the volcanic wall rocks. No crosscutting relationships were observed between E1 and E2 veins. E3 type consists of veins, veinlets, and stringers (<3 cm thick; Fig. 9C) of enargite (chalcopyrite, bornite, tennantite) + pyrite ± quartz. The enargite is massive and has relicts of chalcopyrite, bornite, tetrahedrite, and tennantite. In most cases, E3 veins cut phyllic alteration zones and have no halos, but a few have kaolinite + quartz or thin quartz halos. Enargite and pyrite grains occur disseminated in proximity to the veins. Bornite, recognized inside E1 veins and in their halos, is relict and is replaced by tennantite and enargite. E3 veins cut A, D, E1, and E2 veins. E3 veins cut porphyry 4 and the wall rocks in the central orebody (Fig. 8). In the east orebody, only few examples of this vein cut porphyry 2 at depth. In the sections studied, they occur between 3,200 and 3,800 m.a.s.l., at shallower depths than E1 and E2, showing no crosscutting relationship with E1 veins. E4 veins consist of quartz ± sphalerite ± pyrite and galena veinlets (Table 1; Fig. 9D). Grains of sphalerite (0.6 mm) are intergrown with subhedral quartz crystals (<1 mm). These veins were intercepted by the drill hole ALD-4 in the east orebody at 444-m depth and in the drill hole ALD-43 of the central orebody. They cut porphyries 2 and 4 with phyllic alteration and A and D veins. Anhydrite ± fine-grained quartz ± calcite veins are also associated with this late stage of veins (Table 1; Fig. 9E). They commonly reopen D2 veins and occur in fractures associated with E4 veins. Anhydrite is typically replaced by gypsum (Fig. 9F).

Alteration and Mineralization in the Epithermal Au (Ag-Cu) Siliceous Ledges

The ridges that surround the Altar east orebody are cut by numerous siliceous ledges 1 to 3 m thick that crop out at the surface (Fig. 9G). They are restricted to the high topographic levels (greater than 3,600 m.a.s.l.) cutting the porphyry 1. Most siliceous ledges define a radial arrangement around the east orebody porphyry center. Siliceous ledges also crop out on the ridges that surround the central orebody cutting the tuff of the lower volcanic complex, but there they are scarce. These siliceous ledges have been interpreted as the basal part of an advanced argillic lithocap (Peregrine Metals Ltd., 2011). Most of the ledges consist of chalcedony ± gold with an inner quartz + alunite ± rutile alteration halo, followed by an intermediate quartz + kaolinite zone and an outer chlorite + epidote + calcite halo. Other ledges consist of quartz ± alunite ± enargite ± barite ± gold with thicknesses up to 80 cm (Fig. 9H). This association also occurs as microveinlets that cut the rocks with advanced argillic alteration and fills the open spaces of the vuggy quartz where there is generally native sulfur (Fig. 9I).

TABLE 6. Deposit-Scale Distribution of Fluid Inclusion Types Showing the Relative Abundance of Inclusions in 12 Selected Samples

Location	Sample no.	Depth below surface (m)	Elevation[1]	Vein mineral/ alteration type	Cu grade (wt %)	Mo grade (ppm)	Au grade (ppm)	Fluid inclusion types (%)					Raman analyses
								B30	B20H+	B20H	B90	B20	
Siliceous ledges	ALD-102	Surface	4,042	Quartz/advanced argillic	n.a.	n.a.	n.a.	0	0	0	0	100	n.a.
Siliceous ledges	ALD-102	Surface	4,042	Barite/advanced argillic	n.a.	n.a.	n.a.	0	0	0	80	20	n.a.
Central orebody	ALD-30-32	32	3,673	D2/phyllic	0.08	0	1.35	0	0	18	46	40	n.a.
Central orebody	ALD-46-89	89	3,515	A1/potassic	1.28	18	0.06	2	3	21	73	0	n.a.
Central orebody	ALD-53-111	111	3,485	E1	4.58	8	0.93	26	15	25	27	0	CO_2, HS
East orebody	ALD-14-413	413	3,384	D2/phyllic	0.02	0	3.31	0	33	8	59	0	n.a.
Central orebody	ALD-46-261	261	3,343	A1/potassic	0.44	1	0.06	13	31	15	40	0	n.a.
Central orebody	ALD-46-300	300	3,304	A1/potassic	0.45	5	0.10	5	52	9	33	0	n.a.
Central orebody	ALD-57-672	672	2,938	A1/potassic	0.52	42	0.03	34	16	30	21	0	n.a.
Central orebody	ALD-55-635	635	2,911	B	0.28	28	0.02	45	10	8	37	0	n.a.
Central orebody	ALD-43-730	730	2,905	A1/potassic	0.92	9	0.03	44	26	11	19	0	CO_2
Central orebody	ALD-43-788	788	2,847	B/potassic-phyllic	1.30	20	0.06	48	24	14	14	0	n.a.
Central orebody	ALD-43-869	869	2,766	A1/potassic	0.87	11	0.02	53	23	8	16	0	n.a.

[1] Elevation (m) relative to sea level; Cu, Mo, and Au grade analyses performed by Minera Peregrine Argentina S.A.-Stillwater Mining Company (2-m samples from drill holes)

CL Textures of Quartz Veins

CL textures and trace elements in quartz were analyzed in 21 vein samples of the Altar deposit, including A, B, C, D, and E type veins (central orebody) and epithermal siliceous ledges (east orebody).

A veins contain the most brightly luminescent quartz of any vein type. These veins are dominated by mosaics of roughly equigranular CL-bright quartz, usually with a homogeneous texture, i.e., lacking growth zones or other internal variations in CL intensity (Fig. 10A). In most A veins, the earliest and most abundant generation of CL-bright quartz is intensely fractured by a later CL-dark quartz. CL-bright quartz contains abundant patches of irregular CL-dark quartz that are connected by anastamosing bands (splatter and cobweb texture of Rusk and Reed, 2002; Fig. 10A, B). In some veins, up to three distinct generations of quartz can be distinguished and, in all cases, progressively later generations of quartz are CL darker than the previous quartz generation (Fig. 10C). CL-bright quartz cutting earlier CL-dark quartz was not observed. Where Fe and Cu-Fe sulfides exist in these veins, they are surrounded by a later generation of CL-dark quartz (Fig. 10C). In some veins, the early CL-bright quartz appears to have rounded and embayed edges against the overgrown CL-dark quartz, suggesting dissolution of CL-bright quartz prior to precipitation of later CL-dark quartz (Fig. 10C). Color CL images show that early CL-bright quartz is dominantly blue, whereas later generations are dominated by red wavelengths.

Quartz CL textures in B-type veins contrast with CL textures in A veins in that B veins are dominated by quartz of intermediate CL intensity, commonly displaying euhedrally zoned quartz with micron-scale growth zones of oscillating CL intensity (Q2 in Fig. 10D). Quartz in B veins consistently luminesces with less CL intensity than in A veins, but with more CL intensity than subsequent veins (see below). Many B veins are fractured by later quartz with lower CL intensity. Molybdenite grains in B veins are not consistently surrounded by any single generation of quartz and may be in contact with quartz of any CL intensity (Fig. 10D-F).

CL textures in a single C hematite-quartz vein analyzed show that the quartz has overall lower CL intensity than CL-bright quartz in early A veins and is similar in texture and intensity to B type veins. The quartz is generally fine grained, has low overall CL contrast, and most grains show some internal growth zoning. There is no significant difference in CL intensity from the edge of the vein to the center, where the hematite is located. However, the quartz in contact with hematite tends to be slightly coarser than quartz at the vein margin.

D veins are characterized by significantly lower CL intensity than A, B, and C veins and internal euhedral growth zones of oscillating CL intensity are common (Fig. 11A). In some D veins, several generations of quartz infill are obvious by various morphologies of crystalline quartz growth; however, D veins lack the abundant late fracturing and splatter and cobweb texture that characterizes A and B veins. D veins are commonly reopened by late anhydrite ± fine-grained quartz veins (Fig. 11B). CL images of this late quartz revealed fine-grained banding textures (Fig. 11C).

TABLE 7. Microthermometric Results of the Different Fluid Inclusion Assemblages Hosted in the Different Vein Types at Different Depths

Drill hole	Depth	Vein type	Alteration type	Host mineral	FI type	Te	TmIce (°C)	ThL-V (°C)	TmHalite (°C)	Salinity (avg, wt % NaCl equiv)	N. inclusions
ALD-43	730	A1-A2	Potassic	Quartz	B30	–61.5 ± 1.5	–2.5 ± 0.5	408.5 ± 2.5 (V)		4.07	3
					B30	–55	–0.8	381 ± 9 (V)		1.32	4
					B20Ha+	52.5 ± 1.5	31 ± 0.1	370 ± 5	260.0	35.31	3
					B20Ha+			322 ± 3	380 ± 0.2	45.33	4
					B20Ha+			362.5 ± 2.5	418 ± 0.1	49.45	4
					B20Ha+			252.5 ± 2.5	340 ± 0.1	41.49	3
					B20Ha+			315 ± 0.5	397.5 ± 0.5	47.11	3
					B20Ha	–60	19.8	435.00	435.00	51.40	2
					B90	–51	–2.3 ± 0.1	430 ± 0.1		3.75	3
					B90		–2	431 ± 7		3.27	5
					B90			480 ± 0.1			2
					B90		–1.9	410 ± 0.5		3.11	3
ALD-57	672	A1-A2	Potassic	Quartz	B30	–61 ± 1	–12.7	367.5 ± 0.5 (L)		16.60	2
					B30	–51	–2.3	402 ± 0.1 (L)		3.75	4
					B30	–61.5 ± 1.5	–2.2 ± 0.1	420 ± 0.1 (L)		3.59	4
					B30		–3 ± 0.1	424 (L)		4.86	2
					B30			499 (L)			2
					B30			365 ± 5 (L)			3
					B30			450 (L)			2
					B30			540 (L)			2
					B30			500 (V)			2
					B20Ha			339 ± 0.1	170.0	30.47	3
					B20Ha			340 ± 6	286 ± 4	37.11	4
					B20Ha			474.0	270.0	35.98	2
					B20Ha			368 ± 2	260 ± 7	35.31	3
					B90	–52	–2.4 ± 0.2	400 ± 0.3		3.92	4
					B90			364 ± 15		3.92	7
					B90		–2.3	310 ± 0.1		3.76	2
					B90			410 ± 5.0			3
					B90			450 ± 0.5			3
					B90			388 ± 4.4			4
					B20		–2 ± 0.3	295 ± 5		3.28	8
ALD-46	261	A1-A2	Potassic	Quartz	B30	–54 ± 2	–28 ± 2				2
					B30	–62.5 ± 0.5	–30 ± 0.1				2
ALD-55	635	B	Potassic-phyllic	Quartz	B30	–62	–2.5 ± 0.2	400.0		4.07	2
					B30	–47 ± 1					4
					B20Ha	–62 ± 1					3
					B20Ha+	–49 ± 1.5					4
					B20Ha+	–61 ± 2					4
ALD-57	551	B	Potassic-phyllic	Quartz	B90	–51.5	–2.4±0.2	428 ± 9		3.92	8
					B90			385 ± 5			3
					B90			420 ± 8			3
					B20Ha+	–48 ± 1		353 ± 2	286 ± 2	37.11	5
					B20Ha+			256 ± 9	375 ± 5	44.82	8
ALD-46	271	D2	Phyllic	Quartz	B90		1.7 ± 1	385 ± 2		2.79	6
ALD-53	111	E1	Advanced argillic	Quartz	B20			275 ± 5 (L)			5
					B20Ha	–57 ± 3	19.8	232.5 ± 1.5	383 ± 1.5	45.60	4
					B20Ha			263 ± 6	318 ± 0.1	39.50	4
					B90			423 ± 7			4
					B90	–62.5	–2	390 ± 6		3.27	6
ALD-46	271	E	Phyllic	Anhydrite	B20		2 ± 0.2	254 ± 0.5		3.28	3
					B20		2 ± 0.3	237		3.28	2
					B20			265 ± 2			3
					B20			270 ± 0.1			4

Notes: avg = average, N. inclusions = number of inclusions in the fluid inclusion assemblage, Te = temperature of the eutectic point, ThL-V = temperature of homogenization to liquid (L) or vapor (V), TmHalite = temperature of melting of halite, TmIce = temperature of ice melting

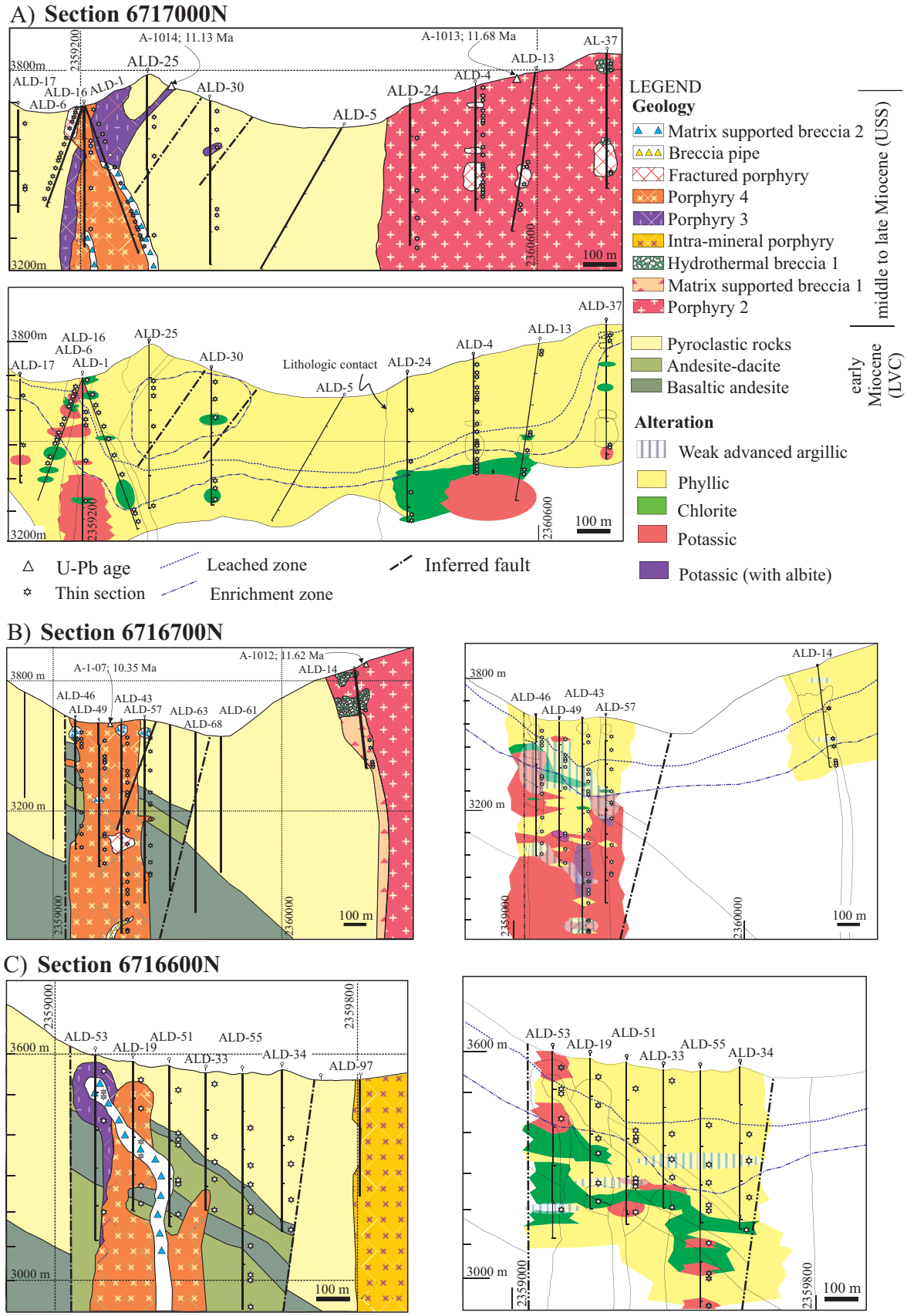

FIG. 4. Geology of the three sections studied with location of drill holes, U-Pb samples, and inferred faults. Locations are given in Gauss Krueguer coordinates, Inchauspe (2).

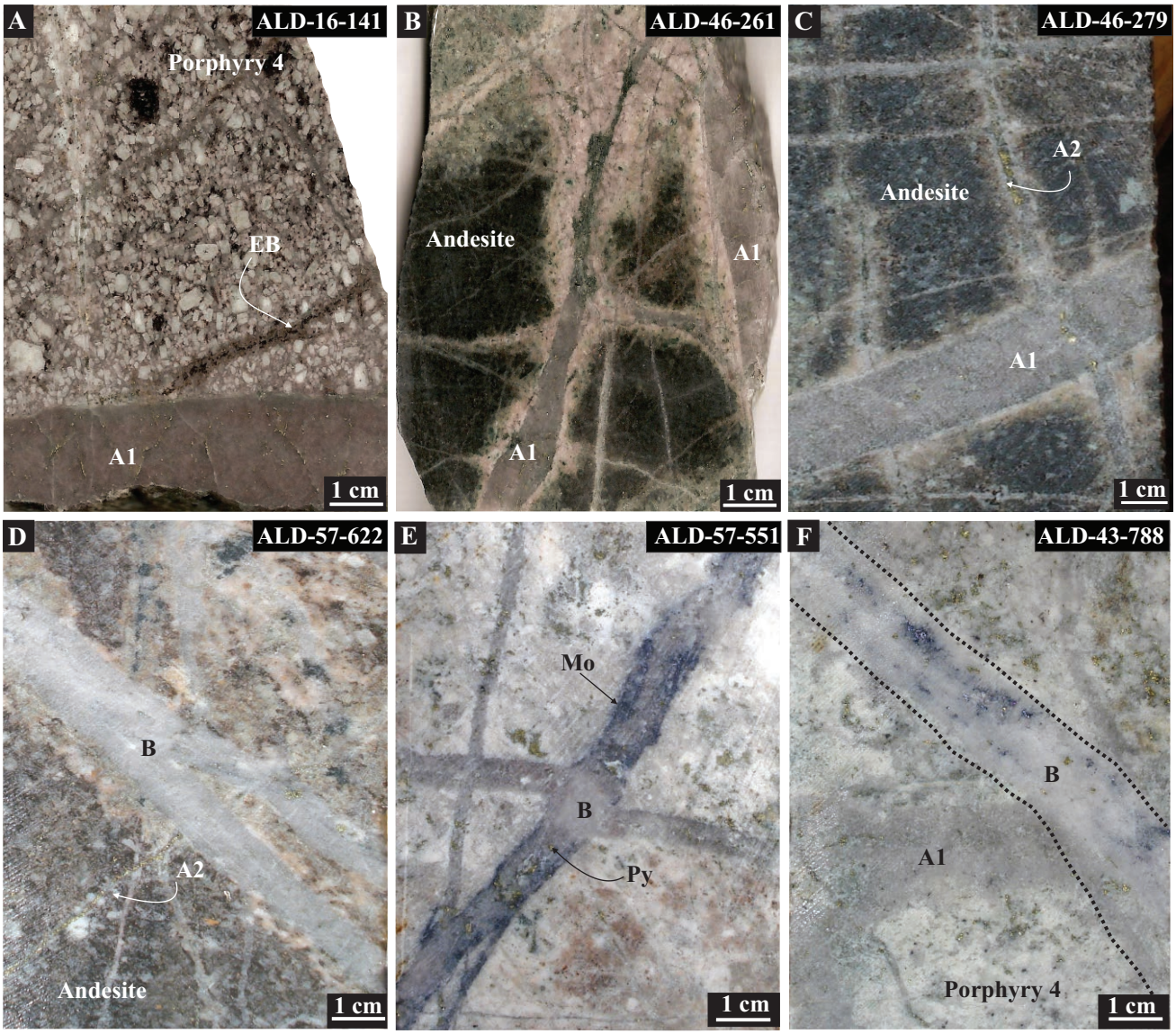

FIG. 5. Representative rock samples of EB, A, and B veins. A) EB vein cut by A1 vein in porphyry 4. B) A1 vein with irregular walls and potassium feldspar + biotite ± rutile halo cut the andesites of the lower volcanic complex. C) A2 veins cut A1 veins in the andesite of the lower volcanic complex. D and E) B veins cut the andesite of the lower volcanic complex. F) B vein cutting A1 vein in porphyry 4 with phyllic alteration.

Later E veins and siliceous ledges display CL textures typical of low and intermediate sulfidation epithermal deposits (Rusk, 2012). These veins are dominated by CL-dark fine-grained quartz with CL banding, as well as ubiquitous euhedral quartz textures with growth zones of oscillating CL intensity (Fig. 11D-G). CL intensity in E veins and siliceous ledges is always lower than CL intensity in A, B, C, and D veins. Splatter and cobweb textures and late CL-dark fractures are absent. These late veins are characterized by one or more generations of euhedral quartz infill and lack the complex textures of fracturing and superposition demonstrated by A and B veins.

Trace Elements in Quartz Veins

Trace elements in 14 lines (tracks; Fig. 12) and ~200 spots from 11 veins were analyzed, including A, B, C, D, and E veins and the siliceous ledges (Fig. 13; Tables 4, 5). Many of these veins contain abundant fluid inclusions, and some contain fine- grained mineral inclusions. Every effort was made to avoid such inclusions, but some contamination in some analyses was inevitable. We monitored a wide range of elements including Na, K, Ca, Mn, Fe, As, Sr, and Pb in order to detect contamination by mineral and fluid inclusions. To determine the effects of fluid inclusions on quantitative analysis of trace elements in quartz, we ablated inclusion-rich quartz from each sample. We found that, whereas fluid inclusions commonly contained significant quantities of Na, K, Mn, Fe, Sr, Pb, and various other elements, Li, Al, Ti, and Ge were not present in significant quantities in any of the analyzed fluid inclusion-rich quartz. In addition to fluid inclusions, some samples contained fine-grained mineral inclusions. A wide variety of mineral inclusions were identified depending on the history and mineral assemblage of each sample. Because

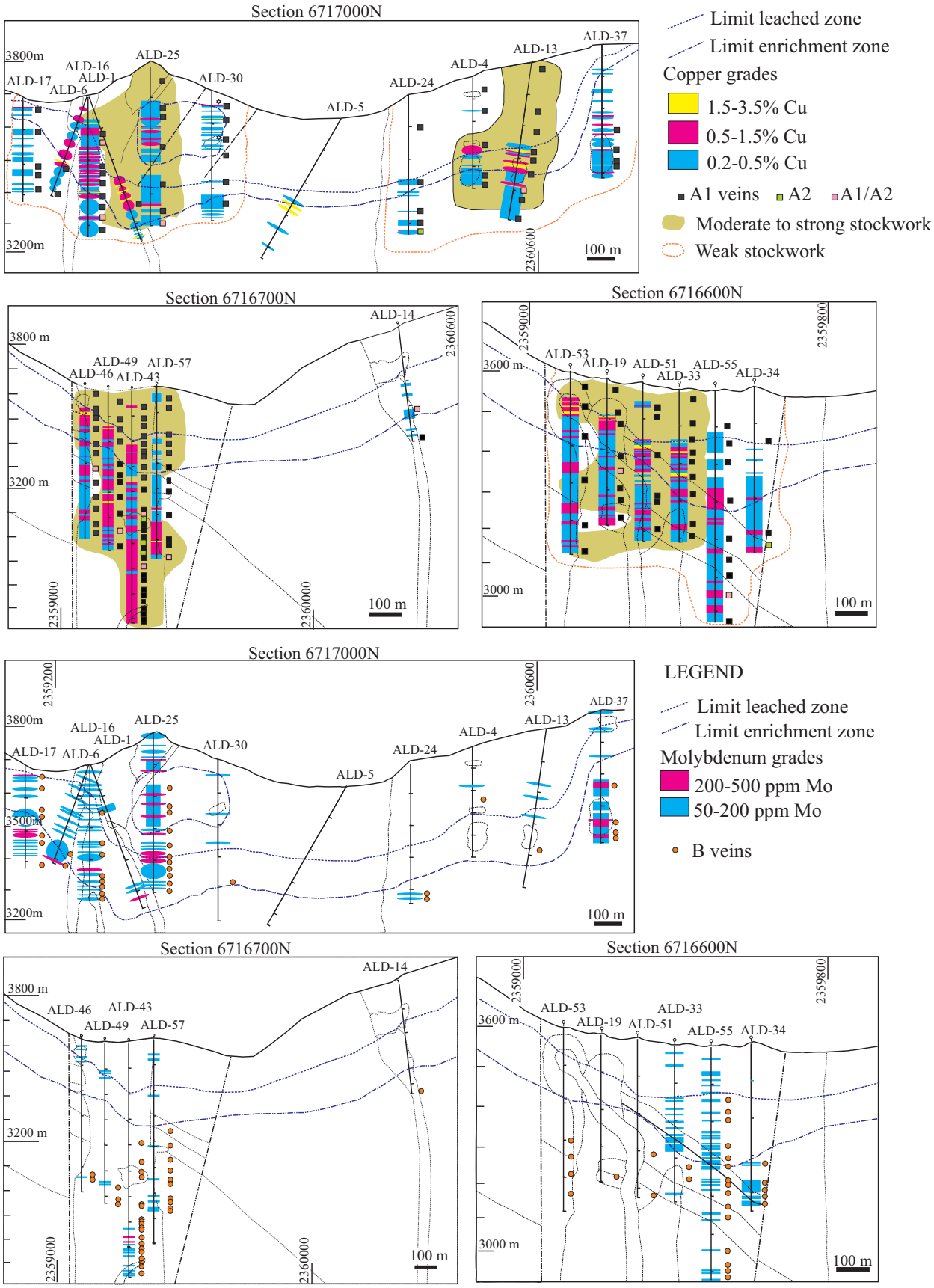

FIG. 6. Distribution of A and B veins: location of weak, moderate, and strong vein stockworks, and Cu and Mo grades.

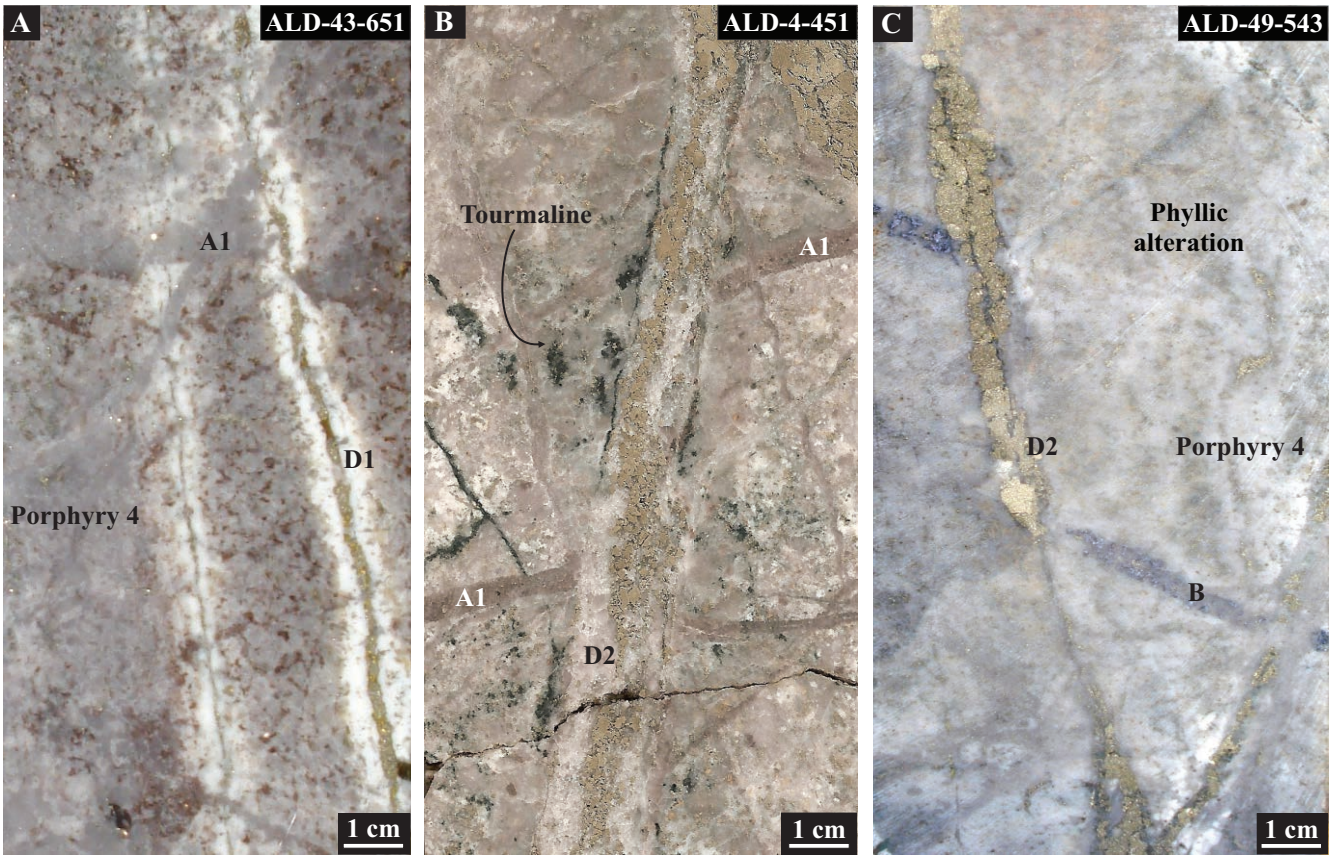

FIG. 7. Examples of D1, D2, and tourmaline veins. A) D1 vein cuts an A2 vein in porphyry 4. B) D2 vein cuts and offsets an A1 vein, associated with tourmaline veinlets. C) D2 vein offsets B vein in porphyry 4.

of the wide and variable contribution of mineral and fluid inclusions in some quartz analyses, conservatively, we present only quantitative data for Li, Al, Ti, and Ge (Tables 4, 5). Of these elements, only Al suffered from occasional contamination from K-Al–bearing inclusions in the quartz—most commonly mica or illite. If any analysis presented contains a small amount of K-Al silicate contamination, then the resultant Al concentration in quartz is a maximum value; however, relatively low total K concentrations in all presented analyses indicate that the contribution of Al from contamination is minor. Inclusions of rutile were only recognized in one vein and the compromised data was discarded. All LA-ICP-MS signals and resultant data were thoroughly scrutinized for the possibility of contamination. Unavoidable contamination was recognized in a small number of total spots (<20) and these analyses were discarded from the dataset.

Only A veins contain CL-bright luminescent mosaics of quartz, although this quartz is frequently cut, fractured, invaded, and overprinted by later CL-darker quartz generations. In most A veins, the scale and intensity of the later overprinting is such that even using LA-ICP-MS, the resolution is not high enough to analyze only a single generation of quartz, so some mixing between quartz generations is unavoidable. In these veins, the elemental trends observed from multiple analyses clarify the quartz compositions.

Early CL-bright quartz of A veins consistently contains more Ti than any other quartz generation, up to ~150 ppm of Ti (Fig. 13A). Aluminum concentrations in A vein quartz are lower than in the rest of the veins, with concentrations mostly between ~50 and 200 ppm. In the highly fractured A vein quartz, Al concentrations overlap with Al concentrations in B, C, and some D vein quartz (Fig. 13A, B). In these same veins, later CL-dark quartz contains much less Ti than the CL-bright quartz and Al compositions vary, but are still below 400 ppm (Table 4). In most A veins, Li concentrations are very low and range between 1 and 5 ppm; however, one A vein, which was reopened by a B vein, has Li concentrations up to ~18 ppm (Fig. 13B, E, F; Table 4), even though the quartz analyzed was more similar to "A vein quartz" than to "B vein quartz." Similarly, Ge concentrations are lowest in A veins, where they range between <1 and 2 ppm (Fig. 13C, D). Germanium concentrations in A veins overlap with B and C veins, but not with D veins or epithermal veins. There is a strong positive correlation between Li and Al in A veins, but in most A veins, there is no strong correlation between any of the other trace elements (Fig. 13A, B).

Quartz in B and C veins has similar CL textures and contains between ~10 and 25 ppm Ti, with Al concentrations between ~50 and 400 ppm (Fig. 13A, Table 4). Ninety % of quartz analyzes of the intermediate-CL quartz from B veins have an average of 20 ppm of Ti (Table 4). Lithium concentrations are slightly higher than in most A veins and range between 2 and 11 ppm (Fig. 13B). There is a weak negative correlation between Al and Ti and a positive correlation between Al and

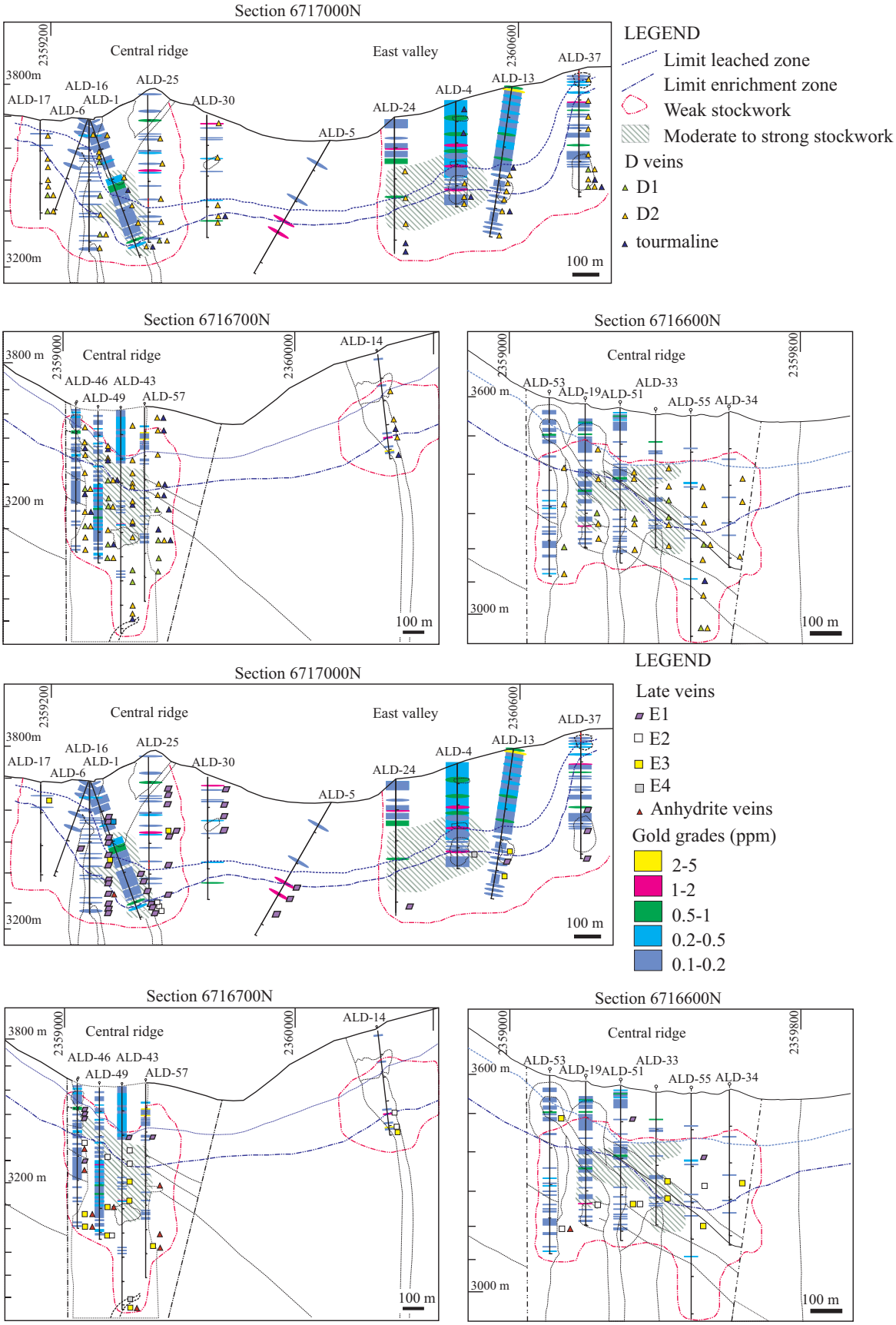

FIG. 8. Distribution of D and E veins, zones of weak, moderate, and strong vein stockworks, and Au grades.

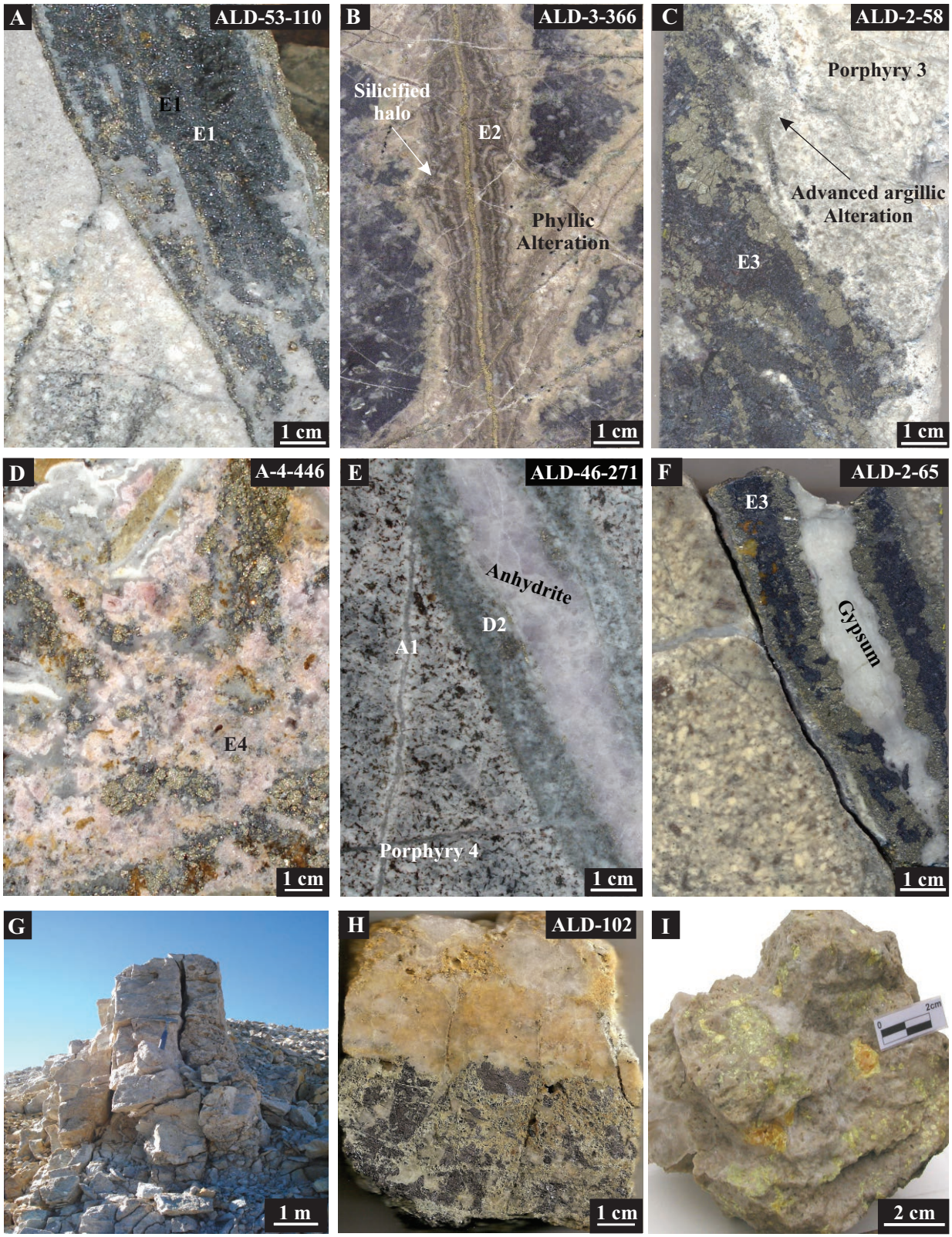

FIG. 9. Examples of E veins and epithermal siliceous ledges. A) E1 vein with tennantite + pyrite. B) E2 vein with silicified halo cuts porphyry 4. C) E3 vein with weak advanced argillic alteration halo hosted in porphyry 3 with phyllic alteration. D) E4 vein (sphalerite + pyrite, galena). E) Late anhydrite ± quartz vein cuts a D vein with phyllic halo. F) Gypsum (after anhydrite) vein cuts an E3 vein. G) Photo of epithermal quartz vein at surface. H) Quartz + enargite ± barite epithermal vein. I) Vuggy quartz with vugs filled with sulfur.

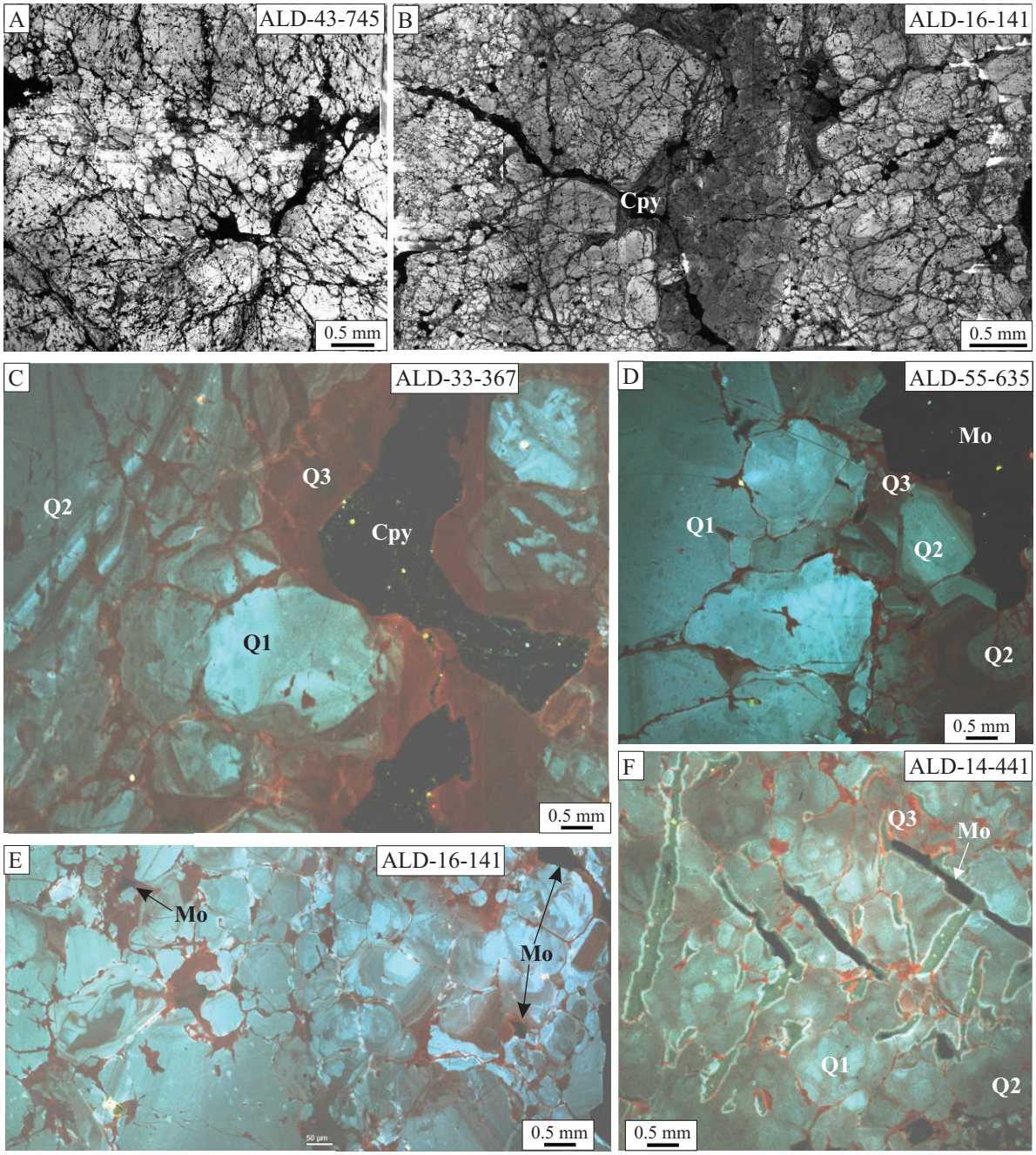

FIG. 10. SEM-CL textures of quartz observed in Altar samples. A) CL-bright quartz in an A vein. B) CL-bright quartz from an A vein cut by later CL-intermediate quartz. C) SEM-CL image of an A1 vein cut by an A2 vein. D and E) CL images of B veins. F) CL image of molybdenite crystals cutting quartz Q1 in the margin of the B vein.

Li (Fig. 13A, B), but Ge is relatively consistent between ~0.8 and 1.5 ppm with no correlation with any of the other elements (Fig. 13C, D). No consistent trends from vein edge to vein center were recognized in B or C veins.

D veins contain lower Ti concentrations, between ~4 and 16 ppm, than the earlier vein types. Al concentrations in D veins range from several hundred ppm up to ~1,700 ppm Al (Fig. 13A; Table 5). Unlike in A, B, or C veins, there is a strong negative correlation between Ti and Al in both D veins analyzed (Fig. 13A). Lithium concentrations are between 5 and 30 ppm and display a strong positive correlation with Al (Fig. 13B). Germanium ranges from 2 to 7 ppm and is also moderately well correlated with the other elements (Fig. 13C, D, F).

E veins contain Ti concentrations from <1 to 10 ppm, with the majority of the analyses below 4 ppm Ti (Fig. 13A; Table 5). On the other hand, in both samples Al concentrations vary widely from ~100 to ~2,500 ppm (Fig. 13A, B). In only one sample, paragenetically the latest vein analyzed (E4), such high Al concentrations are correlated with very high concentrations of Li as reported in several epithermal deposits

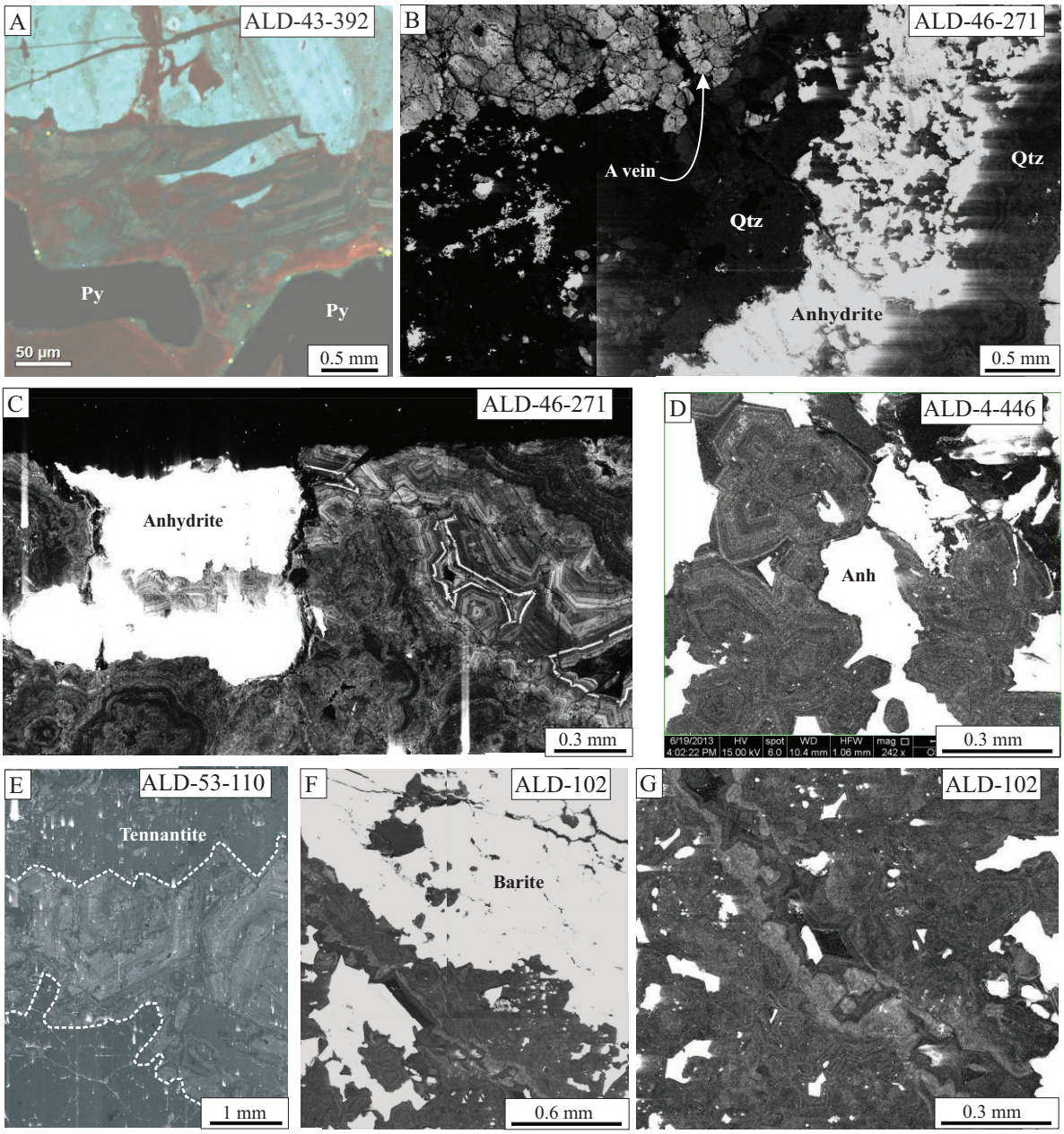

FIG. 11. A) Pyrite in contact with CL-dark quartz with euhedral growth zones in a D2 vein. B) Late anhydrite ± quartz vein cuts an A2 vein. C) Fine-grained banded texture in a late anhydrite ± quartz vein. D) Crystalline euhedral quartz textures in an E4 vein. E) Euhedral quartz zoning in an E1 vein. The tennantite fractures the quartz and indicates reopening in this vein. F, G) CL-dark quartz with banding and zoning in the epithermal siliceous ledge.

(Rusk et al., 2011; Fig. 13B). In the other low-temperature vein from the siliceous ledge, however, even where Al concentrations are several hundred to several thousand ppm, Li concentrations are low (<50 ppm; Fig. 13B). The epithermal quartz contains higher Ge concentrations than A, B, and C veins, and the values mostly overlap with concentrations in D veins (Fig. 13C, D, F).

Although some individual samples do not show obvious correlations among the elements, correlations exist among the data when considering all of the quartz types together. For example, although there is not a strong correlation between Al and Ti values in any samples except for the D veins, over all the analyses, there is a negative correlation between Al and Ti concentrations (Fig. 13). Similarly, there are positive correlations between Al and Ge, Al and Li, and Ge and Li, and negative correlation between Ti and Ge in all samples, although such correlations are not observed in the analyses of single quartz types.

Fluid Inclusion Petrography

Fluid inclusions from veins A, B, D, and E that cut the porphyry 4 in the central Cu-(Au-Mo) Altar orebody were analyzed (Table 6). On the basis of phases present at room temperature, five types of fluid inclusions were distinguished

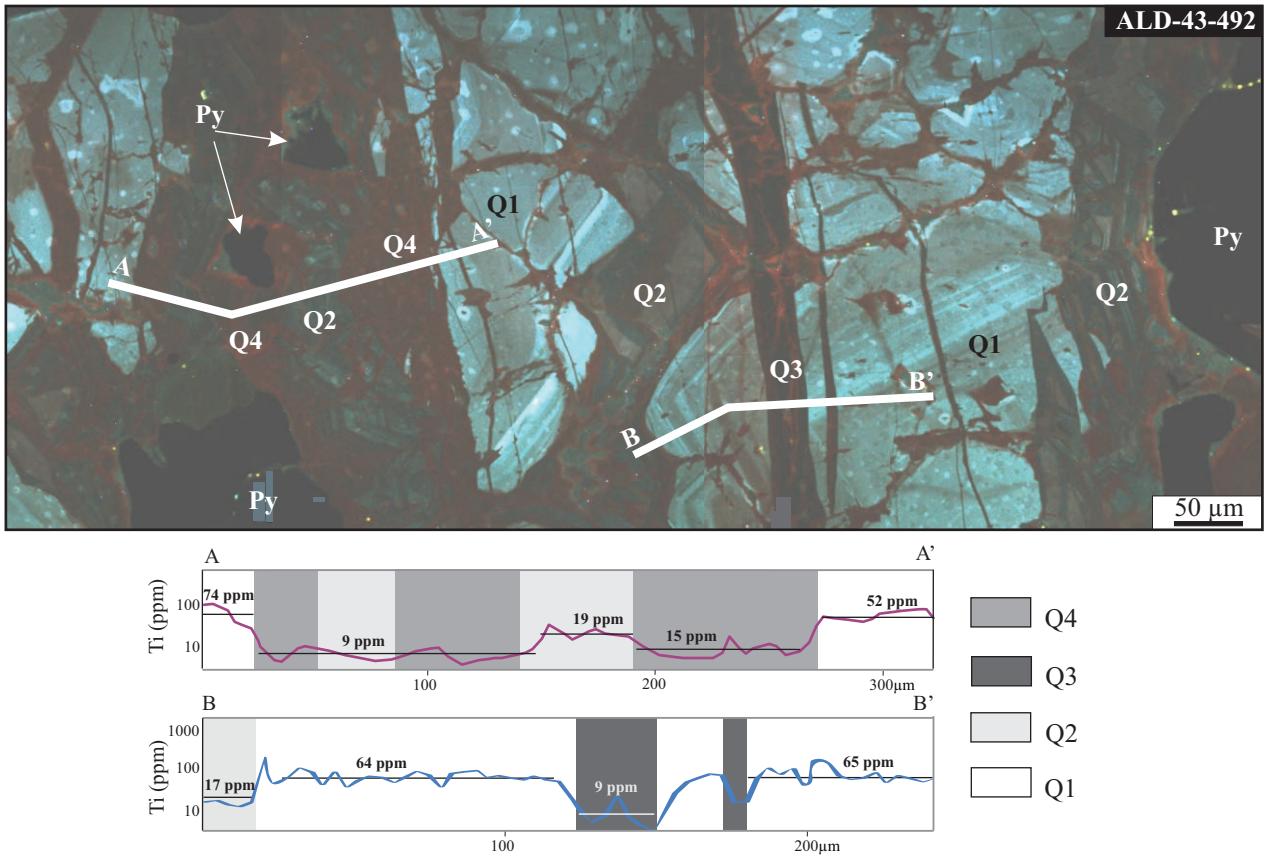

FIG. 12. D2 vein that reopened an A1 vein. Q1 relict of an A1 vein is cut by Q2, in turn cut by Q3 and Q4 quartz. Titanium concentration distribution in the different quartz generations along A-A' and B-B' transects.

using the terminology of Rusk et al. (2008a): B30, B20H+, B20H, B90, and B20, where the letter B denotes bubble, and the number indicates the volume % occupied by the bubble (vapor) in inclusions of that type. The letter H refers to the presence of halite as a daughter mineral and H+ indicates the presence of halite in addition to other daughter phases.

Fluid inclusions were classified as assemblages (Goldstein and Reynolds, 1994), and the data is reported as averages within the assemblage (Table 7). As in most porphyry systems, unequivocal evidence for a primary origin was rarely observed (Wilkinson et al., 2013). Fluid inclusions that occur as individual inclusions and random groups in quartz crystals were interpreted as primary in origin, whereas those aligned along microfractures in trails were designated secondary or pseudosecondary. Most inclusions are between 10 and 50 μm in diameter and have regular or negative crystal shapes. Where possible, inclusion types were linked to specific quartz generations (Fig. 14), based on transmitted light and SEM-CL observations.

B30 fluid inclusions contain liquid and a vapor bubble that occupies 30 to 50 vol % of the inclusion at room temperature (Fig. 14A). Most B30 inclusions are grouped in clusters in individual quartz grains and have negative crystals or rounded forms. Approximately 30% of B30 inclusions contain an opaque and/or a transparent daughter mineral. Traces of CO_2 in the gas phase were only detected in a few cases by Raman spectrometry, but on freezing, neither solidification of liquid CO_2 nor nucleation of a clathrate was detected.

B20H+ inclusions contain multiple daughter minerals, including halite and commonly including sylvite, chalcopyrite, and hematite, based on crystal habits and color (Fig. 14B-F). They are between 25 and 50 μm in diameter and have irregular, regular, or negative crystal shapes.

B20H inclusions contain liquid plus 10 to 20 vol % vapor plus halite at room temperature (Fig. 14G). Ninety % of B20H inclusions also contain one crystal of red hexagonal hematite daughter mineral or one opaque crystal.

B90 inclusions contain more than 80 vol % vapor at room temperature (Fig. 14B). B90 inclusions are typically scattered or occur in clusters within quartz grains. Approximately 50% of B90 inclusions contain an opaque daughter mineral. Nearly all B20H and B20H+ inclusions occur in quartz that also contains B90 inclusions. B20 inclusions contain liquid and 10 to 20 vol % vapor at room temperature (Fig. 14J) and about 20% of B20 inclusions contain one opaque daughter mineral.

Deposit-scale distribution of fluid inclusions

Estimated abundance of each type of inclusion was analyzed in 12 samples from different depths of the deposit (Table 6) along with the vein and alteration type, sample location, and the Cu, Au, and Mo grades of the 2-m interval from which the sample came. The proportions of different fluid inclusion assemblages in each sample analyzed were estimated using a Camera Lucida in five sectors of each vein, drawing a total of 200 fluid inclusions.

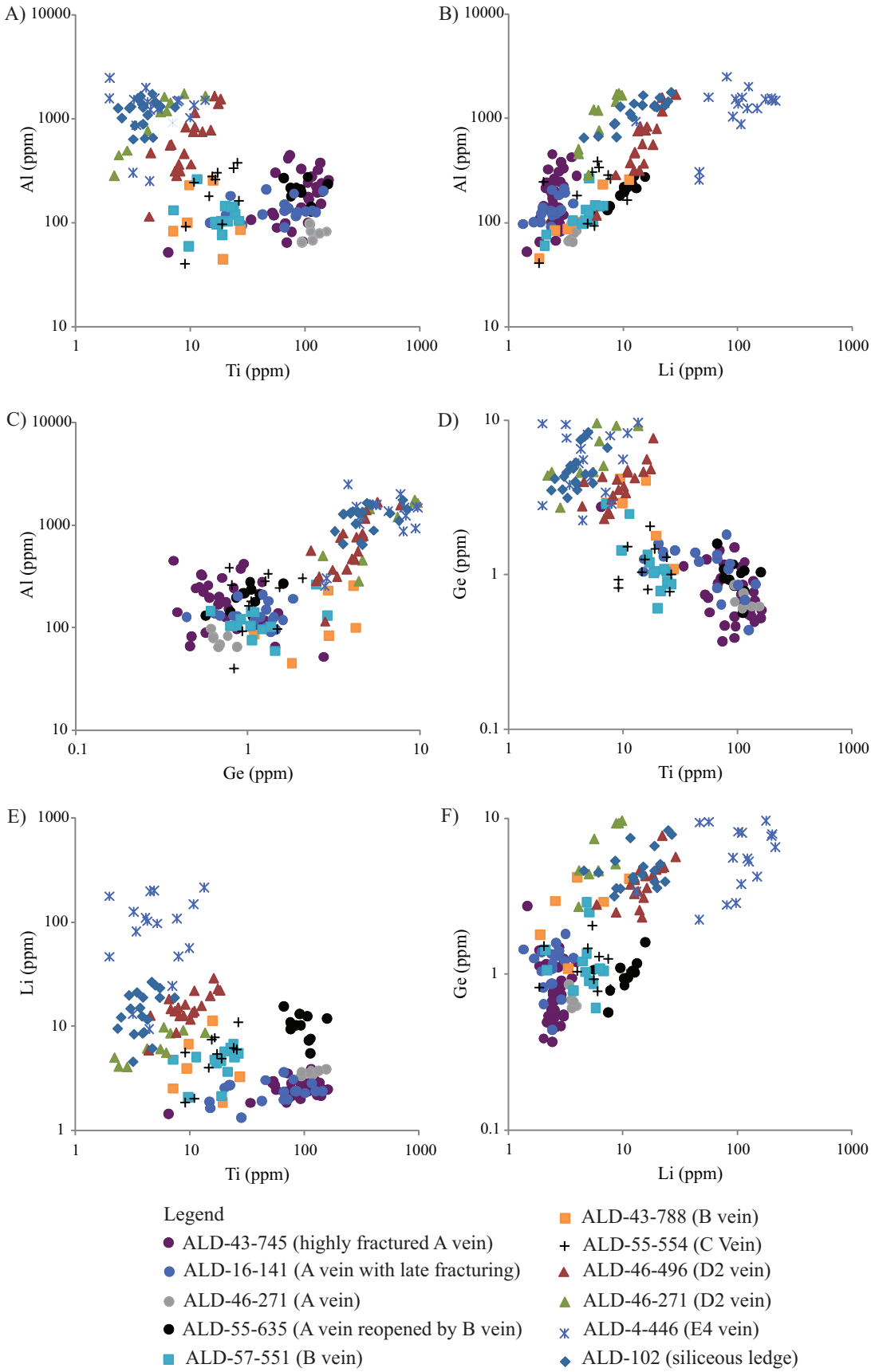

FIG. 13. Concentrations of Ti, Al, Ge, and Li in the quartz from different vein generations (see text for explanations).

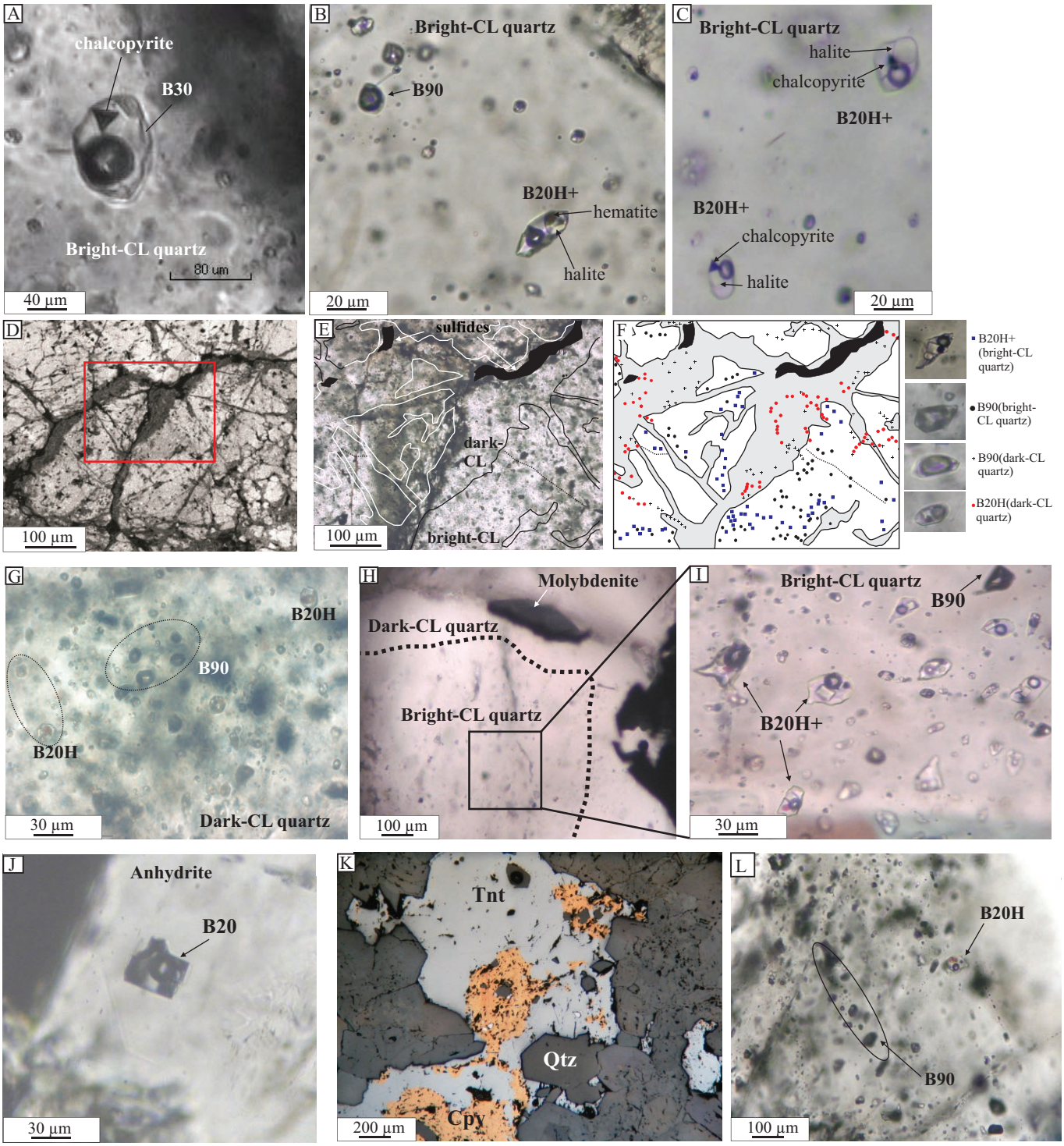

FIG. 14. A) B30 fluid inclusions containing ~50 vol % bubble and a triangular opaque daughter mineral. B) Brine (B20H+) and vapor (B90) inclusion assemblages within CL-bright quartz from an A1 vein. C) B20H+ fluid inclusion assemblages within CL-bright quartz. (D) Example of mapping of the fluid inclusion assemblages in A1 veins. (E) Same region with transmitted light and fluid inclusion assemblages. (F) Sketch of relationship between CL-bright and CL-dark quartz and fluid inclusion assemblages. G) Brine (B20H) and vapor (B90) inclusion assemblages within CL-dark quartz. H) Molybdenite in a B vein. I) Brine (B20H+) and vapor (B90) inclusion assemblages within CL-bright quartz of a B vein. J) B20 fluid inclusion assemblages within anhydrite of late anhydrite ± quartz veins. K) Quartz analyzed from an E1 vein. L) B90 and B20H inclusions assemblages from the E1 vein analyzed.

Early CL-bright quartz of A and B veins contains abundant B30, B20H, and B20H+, but only few B90 inclusions (Fig. 14A-F). B30 inclusions are abundant in A and B veins from the deepest samples (ALD-43-869, ALD- 43-788, ALD-43-730) at about 800 to 600 m below the present surface, where they represent between 30% and 50% of the entire inclusion population. At about 300 m below the present surface, its proportion decreases to less than 15% and at 100 m to less than 5% of the inclusions (Table 6).

B20H and B20H+ are abundant in A and B veins (Figs. 14D-I). In the deepest samples recovered (about 800 m below the present surface), they represent 30% to 50% of the inclusion population (Table 6). In deep A and B veins, B90 inclusions represent 20% to 30% of the inclusion population (Table 6). At 300 m below the present surface, the proportion of B20H and B20H+ increases, representing 60% of the inclusion population, and also the proportion of B90 inclusions increases (40%–60% of the inclusion population). Trails of B20H+ and B90 inclusions were recognized in A and B veins. In A veins from shallow depths (less than 100 m below present surface), B90 inclusions represent 70% of total inclusions.

D2 veins host between 30% and 40% of B20H and B20H+ inclusions (Table 6). Some D2 veins, located 400 m below the present surface, contain 60% of B90 inclusions. At shallow depths (100 m below present surface), D2 veins are dominated by aqueous B20 inclusions (Fig. 14J). In general, E1, E2, and E3 veins lack quartz. However, the E1 vein analyzed contains quartz that hosts B30, B20H+, B20H, and B90 fluid inclusions (Table 6, Fig. 14K, L). Although the quartz of the E1 vein is weakly fractured by the tennantite, it has low CL intensity and is euhedrally zoned (Fig. 10G), showing that it does not belong to an early A or B vein. Epithermal veins (late quartz + anhydrite veins, E4 veins, and siliceous ledges) contain only aqueous B20 inclusions.

Microthermometry

Fluid inclusions in A veins

Seventy % of B30 inclusions from A veins homogenize to liquid between 365° and 420°C, with a mean of 405°C. Inclusions within individual clusters typically homogenize within 0.1° to 5°C of one another. Few B30 inclusions homogenize to vapor between 381° and 500°C (average of 412°C; Table 7; Fig. 15A). Their eutectic temperatures are between –51° and –61°C (average of –58°C). Ice melting temperatures in 75% B30 fluid inclusions occur between –3.0° and –2.2°C (average of –2°C), with corresponding salinities between 3.6 and 4.9 wt % NaCl equiv.

Of all B20H+ inclusions, 85% homogenize by halite dissolution above the temperature of L-V homogenization (Fig. 15B). Halite dissolution temperatures range from 260° to 418°C (Table 7; Fig. 15B) and L-V homogenization occurs between 252° and 370°C. Halite dissolution occurs at temperatures up to 88°C higher than bubble homogenization. Halite melting temperatures in B20H+ reflect salinities between 35.3 and 49.4 wt % NaCl equiv.

B20H inclusions homogenize to liquid between 340° and 474°C (average of 371°C). Halite dissolution occurs first at temperatures that range from 170° to 435°C (average of

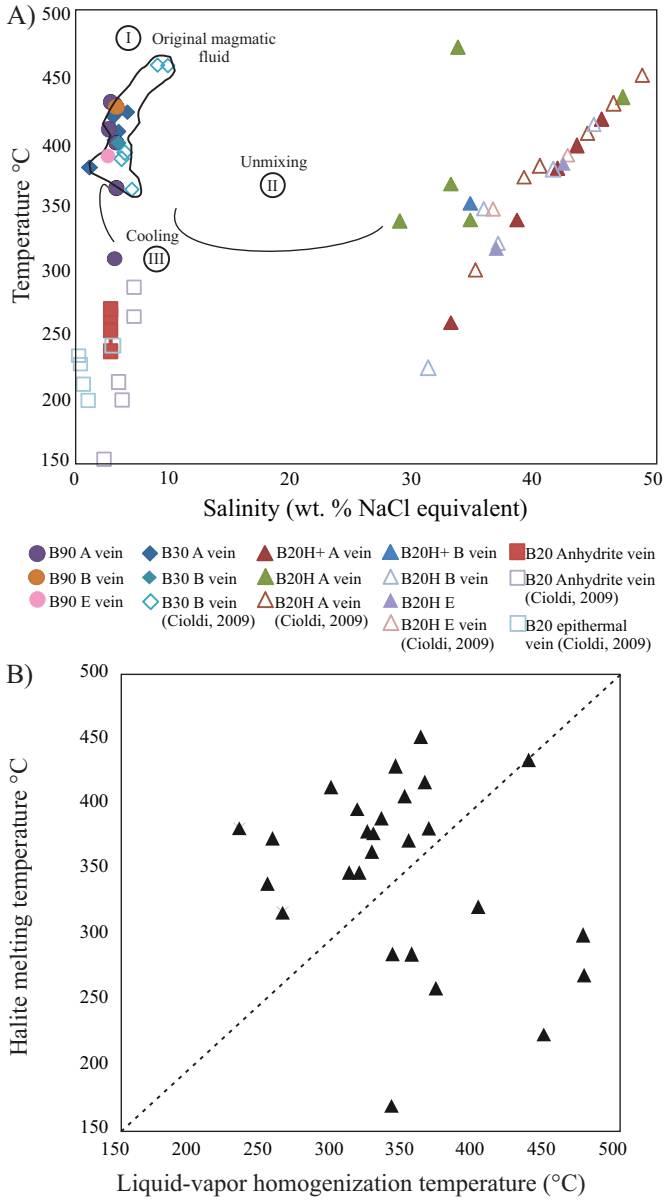

FIG. 15. A) Temperature versus salinity (wt % NaCl equiv) for Altar fluid inclusion assemblages analyzed in this work and in Cioldi (2009). The original magmatic fluid (B30) that exsolved continuously from the magma underwent episodes of unmixing and cooling (registered in A, B veins). Late anhydrite ± quartz veins and epithermal veins formed from lower-temperature fluids. B) Halite melting temperature versus liquid-vapor homogenization temperature for Altar brine inclusions.

270°C, Table 7) and reflect salinities between 30.4 and 51.4 wt % NaCl equiv.

Eighty-five % of B90 inclusions homogenize to vapor between 364° and 450°C (average of 403°C, Table 7) and their ice melting temperatures are between –1.9° and –2.4°C, indicating salinities between 3.1 and 3.9 wt % NaCl equiv.

Fluid inclusions in B veins

B30 fluid inclusions in B veins homogenize to liquid at 400° ± 1°C. Ice melting temperatures occur at –2.5 ± 0.2°C and reflect salinities of 4.1 wt % NaCl equiv (Table 7). Sixty % of

B20H+ inclusions homogenize by halite dissolution at 375° ± 5°C and bubble homogenization occurs at 256° ± 9°C, reflecting salinities of 44.8 wt % NaCl equiv. In these inclusions, halite dissolution occurs at temperatures up to 119°C higher than bubble homogenization. Forty % of B20H+ inclusions homogenized to liquid at 353° ± 2°C with temperatures of halite dissolution at 286° ± 2°C that indicate salinities of 37.1 wt % NaCl equiv. B90 inclusions homogenize to vapor between 385° and 428°C (average of °C, Table 7) with ice melting temperatures of –2.4° ± 0.2°C that reflect salinities of 3.9 wt % NaCl equiv.

Fluid inclusions in D and E veins

B90 inclusions in D2 veins homogenize to vapor at 385° ± 2°C with ice melting temperatures of –1.7° ± 1°C that reflect salinities of 2.7 wt % NaCl equiv. The cores of quartz crystals of the E1 vein sample analyzed contain abundant B90 and B20H inclusions along mineral growth zones (Fig. 14L). B90 inclusions homogenized to the vapor phase at temperatures between 390° and 423°C (average of 406°C, Table 7) with final ice melting temperatures of –2.0°C (salinities of 3.3 wt % NaCl equiv). B20H inclusions homogenized by dissolution of halite from 318° to 383°C (average of 350°C, Table 7), and bubble homogenization occurs between 232° and 263°C. Halite dissolution of B20H indicates salinities of 39.5 and 45.6 wt % NaCl equiv. Late B20 inclusions in these veins homogenize to liquid at 275° ± 5°C. Anhydrite crystals from late anhydrite ± quartz veins host primary B20 inclusions with regular and rectangular shapes (10–40 μm). The B20 inclusions homogenized to liquid at temperatures between 237° and 270°C (average of 259°C, Table 7). Their ice melting temperatures of 2.0 ± 0.3°C (Table 7) reflect salinities of 3.3 wt % NaCl equiv. Quartz of E4 veins contains only very small B20 inclusions. Attempts to analyze them were not successful due the small size of the fluid inclusions.

Discussion

Pressures and temperatures of vein formation

Intermediate-density B30 inclusions that homogenized at high temperatures are abundant in early A and B veins from the deepest samples analyzed (30%–50% of the inclusion population, Table 6). In samples from intermediate levels, the proportion of B30 inclusions decreases whereas the proportion of inclusion assemblages of B20H, B20H+, and B90 increases (and together constitute 75%–95% of the inclusion population). This distribution of fluid inclusions with respect to depth at the deposit scale (Table 6) and the characteristics of B30 inclusions (Fig. 15A; Table 7) suggest that B30 inclusions represent a parental magmatic fluid exsolved from the magma, trapped above its solvus. The increment of the proportion of brine inclusions (B20H and B20H+) and vapor-rich (B90) inclusions at intermediate levels indicates that they were generated by unmixing of the parental low-salinity magmatic fluid represented by the B30 inclusions.

Homogenization by halite dissolution after bubble disappearance was observed in 70% of measured B20H and B20H+ inclusions (Table 7). Such homogenization behavior is relatively common in magmatic hydrothermal ore deposits (e.g., Dilles and Einaudi, 1992; Cline and Bodnar, 1994; Rusk et al., 2008a) and may result from high trapping pressures (Becker et al., 2008). At Altar, halite homogenization occurs at temperatures well above homogenization of the bubble in B20H+ inclusions, suggesting postentrapment modification. Thus, this type of inclusion cannot give a meaningful estimation of P-T conditions (Audétat and Günther, 1999).

To calculate the pressure and temperature conditions of the fluids in each vein stage, the isochores of the fluid inclusion assemblages for each quartz generation were combined with the Ti-in-quartz data (Tables 4, 5) of the same quartz. The intersection of the minimum and maximum Ti-in-quartz isopleths (Huang and Audétat, 2012) with the corresponding fluid inclusion isochores calculated using the Brown and Lamb (1989) equation constrains the pressure and temperature of vein formation (Fig. 16). Rutile is present in A, B, and D veins and in the halos of all Altar veins, which suggests rutile saturation. Therefore, a TiO_2 activity of 1.0 was assumed in all the Ti-in-quartz geothermometry calculations. The area of intersection of the isochores (~90% of the isochores) with the lower and upper Ti isopleths that account for ~90% of the data is shown in dark gray color and the rest of the data is shown in light gray (Fig. 16).

CL-bright quartz with homogeneous texture and very high Ti contents that hosts B30 fluid inclusions corresponds to the earliest quartz generation in A veins. The isochores of B30 inclusions and the Ti isopleths (minimum Ti concentration: 75 ppm Ti; maximum Ti concentration: 130 ppm Ti) in the CL-bright quartz of A veins (Table 4; Fig. 16) indicate trapping conditions of 670° to 730°C and 1.6 to 1.8 kbar for the first quartz generation of A veins. At temperatures above ~400°C, where rock deforms plastically (cf. Fournier, 1999), lithostatic pressures are expected. We therefore infer that deep A veins formed at depths of 6 to 6.8 km, based on lithostatic pressures and rock densities of ~2.7 g/cm^3.

B veins also host B30 fluid inclusions with similar characteristics of B30 inclusions from A veins. The intersection of B30 isochores with the isopleths of 19 ppm of Ti and 27 ppm Ti (minimum and maximum Ti concentration in the CL-intermediate quartz generation of B veins; Table 4; Fig. 16) indicates temperatures of 510° to 540°C and pressures of 800 to 1,000 bars for the formation of the B veins, corresponding to depths of 3 to 3.7 km under lithostatic pressures.

The intersection of the B90 isochores from D2 veins with the isopleths of 7 and 13 ppm Ti suggests temperatures of 370° to 425°C and pressures of 200 to 350 bars for the D2 veins (2–3.5-km depth under hydrostatic conditions).

Epithermal veins (E veins and siliceous ledges) contain B20 inclusions and lower Ti concentrations (0.1–5 ppm; Table 5). Cioldi (2009) analyzed a sample of quartz from the epithermal siliceous ledges that host B20 inclusions with homogenization temperatures between 199° and 242°C to the liquid (average of 216°C) and salinities between 0.18 and 1.22 wt % NaCl equiv.

The isochores of B20 inclusions from the late epithermal anhydrite ± quartz veins (E veins) and of the epithermal siliceous ledges only intersect up to the 1 ppm Ti isopleth and the 0.1 ppm Ti isopleth, respectively, and beyond that give unreasonable pressures (Fig. 16). This can be explained by the lack of calibration of the Ti-in-quartz thermobarometer at low temperatures and pressures.

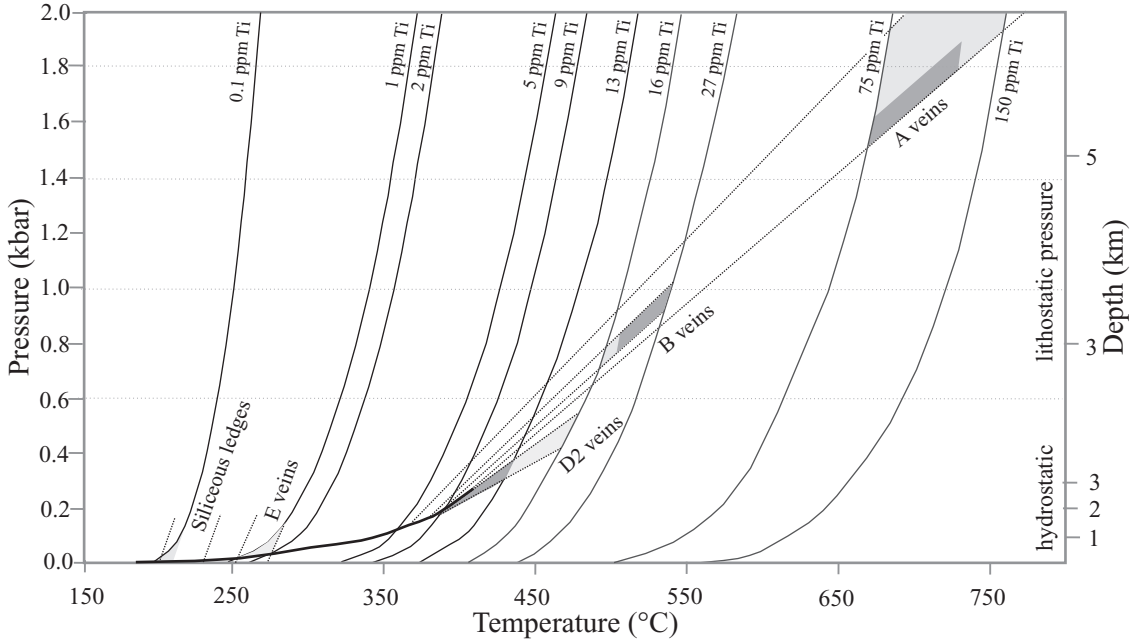

FIG. 16. Pressure-temperature diagram that shows the inferred formation conditions of Altar veins. The regions of intersection of the isochores of the fluid inclusions assemblages (~90% of the data) with the lower and upper Ti isopleths (Huang and Audétat, 2012) that account for ~90% of the Ti-in-quartz data are shown in dark gray areas, and the rest of the data are indicated in the light gray areas. A veins formed at temperatures between 670° and 730°C and lithostatic pressures of 1,600 to 1,800 bars. B veins formed at 510° to 540°C and lithostatic pressures of 800 to 1,000 bars. D veins formed from continued cooling of these fluids in the range of 370° to 425°C and 200 to 350 bars. E veins formed at pressures between 20 and 150 bars and temperatures of 250° to 280°C and epithermal siliceous ledges formed from low-temperature fluids (<230°C) at hydrostatic pressures of <100 bars.

Based on fluid inclusion isochores and knowledge of the geologic environment, E veins formed from fluids at temperatures of 250° to 280°C and pressures of 20 to 150 bars under hydrostatic conditions, considering water density of 1.0 g/cm^3. Siliceous ledges formed from fluids at temperatures of 200° to 230°C at pressures of <100 bars, corresponding to depths of <<1 km.

Ore precipitation mechanisms and distribution

Some textures in A veins suggest dissolution of CL-bright quartz prior to precipitation of later CL-dark quartz (Fig. 11A). According to Kennedy (1950) and Fournier (1999), this process of retrograde dissolution of quartz occurs at temperatures between 550° and 350°C in the presence of low-salinity fluids (<15 wt % NaCl) and pressures under 1,000 bars. Textures similar to these have been observed in other porphyry copper deposits (Butte, Bingham, Oyu Tolgoi, El Salvador, El Teniente, Los Pelambres; Rusk and Reed, 2002; Landtwing et al., 2005; Müller et al., 2010; Rusk, 2012) associated with A veins and Cu mineralization, indicating that the retrograde quartz solubility process may be important to ore formation.

Where Fe and Cu-Fe sulfides exist in A veins, they are in contact with the latest generation of CL-dark quartz (Fig. 11A). Both CL-bright quartz and CL-dark quartz contain B20H (brine) and B90 (vapor-rich) fluid inclusions that are interpreted to reflect unmixing episodes registered in the quartz generations (Fig. 14). The unmixing processes accompanied by a drop in the temperature and/or pressure of the hydrothermal fluids may have led to the Cu-Au precipitation in the Altar potassic core (Drummond and Ohmoto, 1985). In the Bajo de la Alumbrera (Ulrich et al., 2001), Elatiste (Kehayov et al., 2003), and Bingham (Landtwing et al., 2005) porphyry Cu deposits, Au and Cu-Fe sulfide precipitation occurred in response to cooling of a two-phase magmatic fluid (brine and vapor) within a narrow temperature range (420°–340°C) at low pressure (300 bars), where sulfide solubility decreases exponentially, while quartz solubility increases, leading to generation of secondary permeability in previous quartz veins.

In contrast to A veins, B veins are dominated by quartz of CL-intermediate intensity, commonly displaying growth zonation (Fig. 11C, D). In B veins, molybdenite grains are not consistently surrounded by any single generation of quartz and are in contact both with CL-bright quartz and CL-dark quartz (Fig. 11B, C), suggesting a different mechanism for the molybdenite precipitation.

In Altar, high Cu and Au grades are spatially related with the areas of the porphyritic intrusions (Fig. 3B, C). In contrast, the main Mo mineralization is distributed around porphyry 4 and in the wall rocks that surround this intrusion and the main Cu-Au zone (Fig. 3B, C), as is observed in other porphyry deposits (e.g., Saindak, Pakistan: Sillitoe and Khan, 1977; Bajo La Alumbrera: Ulrich and Heinrich, 2001; Proffett, 2003; La Esperanza: Perelló et al., 2004; Agua Rica: Franchini et al., 2011). Compared to A veins, the quartz of B veins has lower Ti concentrations and similar Al, Li, and Ge contents (Fig. 13A-C). The lower concentration of Ti in Altar B veins and the distribution of Mo at the deposit scale (Fig. 3C) suggest that molybdenite precipitated at lower temperatures compared to the first pulse of Cu-Fe sulfides.

The quartz from D veins is characterized by lower CL intensity and has lower Ti contents and higher Al, Li, and Ge concentrations than A and B veins. Concentrations of Ti, Al, and Li of D veins are consistent and show intermediate compositions between A and B vein quartz and E4 vein quartz (Fig. 13B, C). Allan and Yardley (2007) interpret the high Al concentrations in quartz, observed in D veins, as the result of high quartz precipitation rates, triggered by depressurization of the hydrothermal system followed by the influx of cooler meteoric fluids. Rusk et al. (2008b) suggest that higher Al concentrations in epithermal quartz indicate increased Al solubility resulting from a decrease of fluid pH at low temperatures.

In this study (E1 vein) and in Cioldi (2009; E3 vein), E1 and E3 veins were observed to contain high-temperature brine- and vapor-rich inclusions that homogenized between 350° and 400°C. However, the CL images (Fig. 10G) suggest that the quartz formed prior to the sulfosalts, since it is fractured by the tennantite. Thus, the high-temperature fluid inclusion measurements from E1 vein quartz likely reflect the reopening of a previously formed D vein. Sulfosalt-rich E1-E2 and E3 veins overlap the deep and intermediate high-temperature veins in the central ridge and introduced significant Cu and Au mineralization. Part of this Cu-Au may have been leached from the potassic alteration and mineralization. In areas with phyllic alteration, A quartz veins were stripped of former chalcopyrite and bornite, and tennantite, enargite, pyrite, and bornite are disseminated between the quartz veinlets (Peregrine Metals Ltd., 2011). At Altar, the leaching and reprecipitation of the sulfides in high sulfidation associations is similar to hypogene enrichment described at Butte, Montana (Brimhall, 1979).

Late anhydrite ± quartz veins that cut D veins display CL textures similar to epithermal quartz (euhedrally zoned crystals and banded textures that resemble microcrystalline quartz, Fig. 11C). Quartz from E4 veins (associated with a Zn-Pb mineralization pulse; sample ALD-4-446) has CL textures and trace elements very similar to those of quartz from epithermal ore deposits. E4 veins have extreme trace element compositions relative to the other vein types (Fig. 13), consistent with their formation late in the evolution of the system.

A sample of quartz from the epithermal siliceous ledge (ALD-102) contains only CL-dark quartz with zoning (Fig. 10H, I). Along with sample A4-446 (E4 vein), this sample has the lowest Ti concentrations. The quartz in this sample contains high Al and Ge that overlap with E4 veins and with some D vein compositions. However, this quartz has low Li, while epithermal quartz (Rusk, 2012) typically has high Li contents. Lithium contents in Altar may be higher in the fine-grained banded quartz that is absent in the siliceous ledges analyzed (Fig. 13B, E, F).

Evolution of hydrothermal fluids in time and space

Positive correlations between Ti concentration and quartz temperature have been recognized in several porphyry systems (Landtwing et al., 2005; Rusk et al., 2006; Allan and Yardley, 2007; Müller et al., 2010). In Altar early veins, the Ti content decreases through time in a single vein (A and B veins) and it also decreases from early veins (A, B, C) to late veins (D, E), indicating that fluid temperatures decreased through time during the formation of the system.

Vein formation occurred at progressively lower pressure, shallower paleodepth, and lower temperature, as can be observed in Figure 16. Under lithostatic pressures, the magma supplied low-salinity aqueous fluids at depths of ~6 km (pressures of 1.6–1.8 kbar) and temperatures of 670° to 730°C (Fig. 17). These fluids sporadically depressurized at temperatures and pressures below the brine-vapor solvus (Roedder, 1984, 1992; Bodnar et al., 1985; Cline and Bodnar, 1991; Bodnar, 1995), as is indicated by the coexisting B20H and B90 inclusions in A and B veins and, less commonly, in D veins (Fig. 15A).

Cooling of the hydrothermal fluids below ~400°C may have produced pervasive phyllic alteration that overprinted the early hydrothermal assemblages and filled straight-walled veins with phyllic halos (D veins, Fig. 17). These fluids with lower pH and temperature would have partially leached the mineralization from earlier potassic alteration. D veins formed from fluids at 370° to 425°C and 200 to 350 bars under hydrostatic pressures.

Late veins rich in sulfides and sulfosalts (E1, E2, and E3) overlapped the deep and intermediate high-temperature veins and introduced significant Cu and Au mineralization. The assemblage quartz ± alunite ± enargite ± barite ± gold of the epithermal siliceous ledges formed from fluids with temperatures of ~250°C (Seward, 1981; Hedenquist, 1987; Stoffregen, 1987). Sulfide stable isotope data at Altar (Maydagán et al., 2013) indicate the involvement of magmatic fluids in all stages of mineralization. Enargite from the epithermal siliceous ledges has a distinctive lighter $\delta^{34}S$ value consistent with a decrease of temperature, pH, and/or an increase in the oxidation state of the fluids during its deposition (Maydagán et al., 2013). This may be related to a dilution by groundwater (e.g., Cooke et al., 2011) that may have favored the Au and Ag precipitation at epithermal levels (e.g., Corbett and Leach, 1998; Hedenquist et al., 2000; Simmons et al., 2005). Chalcedony ± gold ledges precipitated from low-temperature fluids (<150°C; Corbett and Leach, 1998).

Telescoping of the system

As a result of glacial erosion, Altar reveals the transition between high sulfidation siliceous ledges and the subvolcanic porphyry deposit. On the high ridges of the earlier east mineralized center, numerous epithermal siliceous ledges crop out associated with advanced argillic alteration halos (Fig. 3), whereas at depth, porphyry 2 lacks E veins, except for very few examples (Fig. 8). In contrast, in the younger mineralized center of the central ridge, where few epithermal siliceous ledges crop out, type E veins are very common in porphyries 3 and 4, cutting the early deep, intermediate, and shallow veins (Fig. 8).

Quartz from E veins displays CL textures similar to quartz from low and intermediate sulfidation epithermal deposits (Rusk, 2012). B30 isochores from A and B veins indicate depths of formation of ~6 km for the early A veins under lithostatic pressures. Considering the trace element content and fluid inclusions of the crystalline quartz from the D veins, these veins may have been formed at depths of 2 to 3.5 km (Fig. 17). Thus, after the emplacement of porphyry 4 and during the hydrothermal lifetime of the central orebody, the erosion and exhumation of the land would have been at

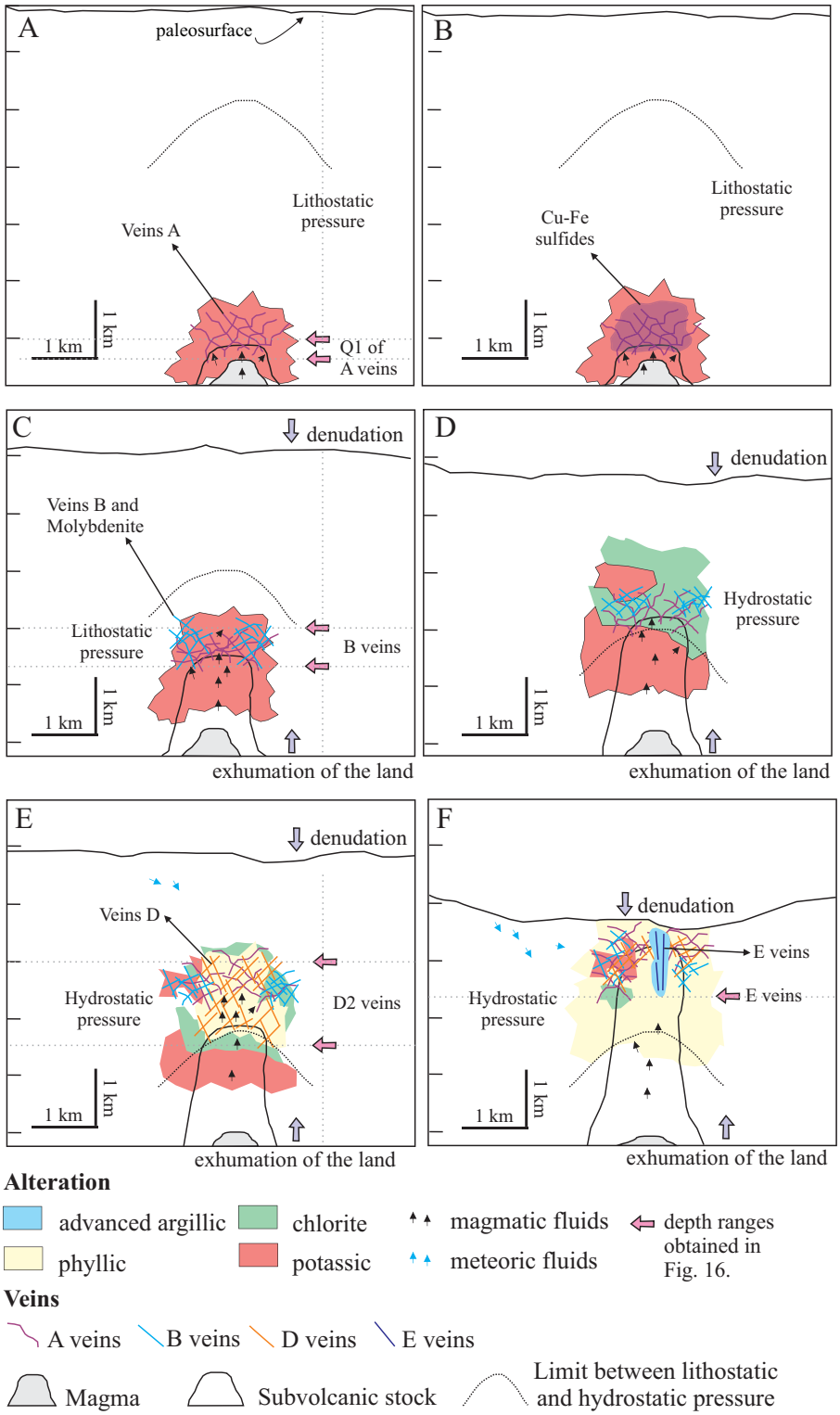

FIG. 17. Schematic diagram of the evolution of the Altar magmatic-hydrothermal system in the central orebody. A) Magmatic fluids were exsolved at high temperatures and lithostatic pressure. At these conditions, B30 fluid inclusions were trapped in early A veins. B) As B30 fluids ascend, they unmix into B20H and B90 fluids associated with fluctuations of the pressure and a decrease of temperature, then Cu-Fe sulfides precipitated in these veins related to the latest quartz generation. C) B veins formed from similar fluids cooling and depressurizing at lower temperatures and pressures. D and E) Fluids cooled below 400°C at hydrostatic pressures, which favored the decrease of their pH, leading to chloritic and phyllic alteration and D vein formation. F) E veins precipitated sulfosalts associated with Cu-Au mineralization at lower temperatures and pressures. The exhumation and denudation of the land during the formation of the Altar hydrothermal system favored late low-temperature veins cutting early high-temperature veins. Pink arrows indicate the depth ranges calculated in Figure 16.

least of ~2.5 km, and would have favored the overlapping of the shallow and deep mineralization in the central orebody. Similar telescoping processes (e.g., Sillitoe and Hedenquist, 2003) have been recognized in other porphyries of the flat slab (Famatina: Pudack et al., 2009, Agua Rica: Franchini et al., 2011, 2012).

The emplacement of the porphyries in the flat-slab segment took place under a compressive regime and crustal shortening associated with high rates of exhumation. North of Altar, in the El Indio-Pascua belt (29°20'–30°30'S), the processes of erosion and exhumation were recorded by the incision of three regional pediplains over the period 17 and 6 Ma (Bissig et al., 2002). The erosional landforms are considered to have formed in a semiarid climate in direct response to uplift events (Bissig et al., 2002). In Los Pelambres deposit, located close to Altar, U-Th/He ages in zircon and apatite of 10.37 to 8.15 Ma indicate a rapid cooling of Los Pelambres stock and its associated mineralization as a result of rapid exhumation during tectonically induced uplift (Bertens et al., 2006). The tilting of the entire Los Pelambres system was synmineral in timing and presumably linked to the tectonic uplift of the region (Perelló et al., 2012), between 12 and 7 Ma (Giambiagi and Ramos, 2002). A jarosite age of 5.34 Ma from the supergene alteration implies that Los Pelambres deposit was already unroofed by the latest Miocene (Bertens et al., 2006).

Telescoping occurs in response to profound surface degradation by uplift-induced erosion or, less commonly, by volcanic collapse during the lifespans of hydrothermal systems (Sillitoe, 1994). Telescoping is controlled by zones of maximum permeability, which were provided by synmineral faults at Chuquicamata (Lindsay et al., 1995) and by a hydrothermal breccia pipe at Agua Rica (Perelló et al., 1998). Other evidence of uplift and erosion in the Altar area is the presence of the roots (basal part) of the epithermal lithocap along the eastern side of the Altar deposit and the complete erosion of the lithocap in the central orebody. Mapping in the northern part of the Altar cirque identified an NE-oriented fault projected to cut the center of the deposit between the central orebody and the east orebody (Peregrine Metals Ltd., 2011). The erosion of the lithocap in the central orebody suggests west-side-up displacement of the central orebody across this fault system.

Conclusions

Altar (995 Mt, 0.35% Cu, and 0.083 g/t Au), located in the Central Andes of San Juan Province, Argentina, is an excellent example of overlapping of porphyry Cu-(Au-Mo) and epithermal Cu-Au veins. The mineralization is associated with three mineralized intrusions and breccias (10–12 Ma) that intruded early Miocene (20–21 Ma) volcanic sequences and formed two magmatic hydrothermal centers with mineralization located in the east valley (the older) and the central ridge (the younger; Fig. 3). Metallic mineralization at Altar porphyry deposit precipitated in three main stages of veins with quartz. The first and second stages are represented by quartz ± chalcopyrite ± pyrite veins (A veins) and quartz ± molybdenite veins (B veins) formed during early alteration at high temperatures and pressures. The third mineralization stage corresponds to late veins rich in sulfides and sulfosalts (E veins) and the siliceous ledges that formed at low temperatures equivalent or transitional to the epithermal environment.

SEM-CL of Altar veins reveals a wide variety of textures that clearly differentiate multiple generations of quartz in the individual veins and relate sulfides to a specific generation of quartz. The CL intensities and textures can be correlated with the different vein generations. The LA-ICP-MS data demonstrate that trace elements in quartz also discriminate between multiple generations of quartz in individual veins and between different vein generations. The combination of CL and trace elements in quartz is critical for deciphering the cryptic relationships between mineralization and alteration events, making it a useful tool for exploration of these systems, especially those with complex superposition of multiple mineralization events.

In the eastern zone of the Altar deposit, epithermal siliceous ledges occur on the high ridges above the porphyry deposit, whereas in the central orebody, epithermal veins (E veins or equivalent to epithermal) overlap the porphyry veinlets. The uplift of the land in the central Altar orebody would have increased the overlapping of late low-temperature and early high-temperature veins. Similar telescoping processes have been recognized in other porphyry deposits of the flat-slab segment (e.g., Famatina: Pudack et al., 2009; Agua Rica: Franchini et al., 2011, 2012).

Acknowledgments

This research represents part of a Ph.D. dissertation completed at the Universidad Nacional del Sur and forms part of a project financed by CONICET (PIP n° 6043 and PIP n° 1083), Minera Peregrine Argentina S.A.-Stillwater Mining Company, a Student Research Grant awarded by the Society of Economic Geologists, and an international cooperation program, CONICET-NSF. We express our appreciation to Jeff Toohey for collaboration with this study, and to Jorge Bengochea, Guillermo Almandoz, and Santiago Gígola (Río Tinto Mining & Exploration) and the staff of Minera Peregrine Argentina S.A. for site access, logistic support, and help during the field work. David Lentz and Chris McFarlane are supported by Natural Sciences and Engineering Research Council Discovery research grants. We thank Dr. Yan Luo (UNB) for helping with the acquisition of the LA-ICP-MS data and Dr. Douglas Hall (UNB) for the Chroma SEM-CL imaging that complemented the LA-ICP-MS analyses. We thank Dr. John Dilles, Federico Cernuschi, and Nansen Olson for helping with the acquisition of CL images at the Oregon State University. We also thank FAPEMIG (Project CRA PPM 00179/13) and CNPq (Project 307546/2011-0), and Dra. Maria Sica Dantas (Eng-Dept-UFMG- Brazil) for the Raman support. We thank Larry Meinert, Murray Allen, and Tim Baker for their constructive reviews that led to further improvement of this manuscript.

REFERENCES

Allan, M., and Yardley, B., 2007, Tracking meteoric infiltration into a magmatic hydrothermal system: A cathodoluminescence, oxygen isotope and trace element study of quartz from Mt. Leyshon, Australia: Chemical Geology, v. 240, p. 343–360.

Anderson, M., Alvarado, P., Zandt, G., and Beck, S., 2007, Geometry and brittle deformation of the subducting Nazca plate, central Chile and Argentina: Geophysical Journal International, v. 171, p. 419–434.

Arribas, Jr., A., Hedenquist, J.W., Itaya, T., Okada, T., Concepción, R.A., and Garcia Jr., J.S., 1995, Contemporaneous formation of adjacent porphyry and epithermal Cu-Au deposits over 300 ka in northern Luzon, Philippines: Geology, v. 23, p. 337–340.

Audétat, A., and Günther, D., 1999, Mobilization and H_2O-loss from fluid inclusions in natural quartz crystals: Contributions to Mineralogy and Petrology, v. 137, p. 1–14.

Becker, S.P., Fall, A., and Bodnar, R.J., 2008, Synthetic fluid inclusions: XVII. PVTX properties of high salinity H_2O-NaCl solutions (>30 wt% NaCl): Application to fluid inclusions that homogenized by halite disappearance from porphyry copper and other hydrothermal ore deposits: Economic Geology, v. 103, p. 539–554.

Bertens, A., Clark, A., Barra, F., and Deckart, K., 2006, Evolution of the Los Pelambres-El Pachón porphyry copper-molybdenum district, Chile/Argentina: Universidad Católica del Norte, Chile, XI Congreso Geológico Chileno, Antofagasta, Chile, 7–11 August 2006, Proceedings, v. 2, p. 179–181.

Bissig, T., Clark, A.H., Lee, J.K., and Hodgson, C.J., 2002, Miocene landscape evolution and geomorphologic controls on epithermal processes in the El Indio-Pascua Au-Ag-Cu belt, Chile and Argentina: Economic Geology, v. 97, p. 971–996.

Bodnar, R.J., 1993, Revised equation and table for determining the freezing point depression of H_2O-NaCl solutions: Geochimica et Cosmochimica Acta, v. 57, p. 683–684.

——1995, Fluid-inclusion evidence for a magmatic source for metals porphyry copper deposits: Mineralogical Association of Canada Short Course Series, v. 23, p. 139–152.

Bodnar, J.R., and Vityk, M.O., 1994, Interpretation of microthermometric data for H_2O-NaCl fluid inclusions, *in* De Vivo, B., and Frezzotti, M.L., eds., Fluid inclusions in minerals: Methods and applications: Blacksburg, VA, Virginia Technical Institute, p. 117–130.

Bodnar, R.J., Burnham, C.W., and Sterner, S.M., 1985, Synthetic fluid inclusions in natural quartz. III. Determination of phase equilibrium properties in the system H_2O-NaCl to 1000°C and 1500 bar: Geochimica et Cosmochimica Acta, v. 49, p. 1861–1873.

Brimhall, G.H., 1979, Lithologic determination of mass transfer mechanisms of multiple-stage porphyry copper mineralization at Butte, Montana: Vein formation by hypogene leaching and enrichment of hypogene protore: Economic Geology, v. 74, p. 556–589.

Brown, P.E., and Hagemann, S.G., 1994, Mac Flincor: A computer program for fluid inclusion data reduction and manipulation, *in* De Vivo, F., and Frezzotti, M., eds., Fluid inclusion in minerals: Methods and applications: Blacksburg, VA, Virginia Polytechnic Institute and State University, p. 231–250.

Brown, P.E., and Lamb, W.M., 1989, P-V-T properties of fluids in the system $H_2O \pm CO_2 \pm$NaCl: New graphical presentations and implications for fluid inclusion studies: Geochimica et Cosmochimica Acta, v. 53, p. 1209–1221.

Cahill, T., and Isacks, B., 1992, Seismicity and shape of the subducted Nazca plate: Journal of Geophysical Research, v. 97, p. 17,503–17,529.

Catchpole, H., Kouzmanov, K., and Fontboté, L., 2012, Copper-excess stannoidite and tennantite-tetrahedrite as proxies for hydrothermal fluid evolution in a zoned Cordilleran base metal district, Morococha, central Peru: Canadian Mineralogist, v. 50, p. 719–743.

Charrier, R., Baeza, O., Elgueta, S., Flynn, J.J., Gans, P., Kay, S.M., Muñoz, N., Wyss, A.R., and Zurita, E., 2002, Evidence for Cenozoic extensional basin development and tectonic inversion south of the flat-slab segment, southern Central Andes, Chile (33°–36° S): Journal of South American Earth Sciences, v. 15, p. 117–139.

Cioldi, 2009, The Altar Exploration Project: Geology and hydrothermal mineralization paragenesis of the Cu-Mo-Au porphyry deposit, San Juan Province, Argentina: Unpublished M. Sc. thesis, Zurich, ETH Zurich, 68 p.

Cline, J.S., and Bodnar, R.J., 1991, Can economic porphyry copper mineralization be generated by a typical calc-alkaline melt?: Journal of Geophysical Research, v. 96, p. 8113–8126.

——1994, Direct evolution of brine from a crystallizing silicic melt at the Questa, New Mexico, molybdenum deposit: Economic Geology, v. 89, p. 1780–1802.

Cooke, D.R., Deyell, C.L., Waters, P.J., Gonzales, R.I., and Zaw, K., 2011, Evidence for magmatic-hydrothermal fluids and ore-forming processes in epithermal and porphyry deposits of the Baguio district, Philippines: Economic Geology, v. 106, p. 1399–1424.

Corbett, G.J., and Leach, T.M., 1998, Southwest Pacific rim gold-copper systems: Structure, alteration and mineralization: Society of Economic Geologists, Special Publication 6, 236 p.

Deyell, C., and Hedenquist, J., 2011, Trace element geochemistry of enargite in the Mankayan district, Philippines: Economic Geology, v. 106, p. 1465–1478.

Dilles, J.H., and Einaudi, M.T., 1992, Wall-rock alteration and hydrothermal flow paths about the Ann-Mason porphyry copper deposit, Nevada, a 6-km vertical reconstruction: Economic Geology, v. 87, p. 1963–2001.

Drummond, S.E., and Ohmoto, H., 1985, Chemical evolution and mineral deposition in boiling hydrothermal systems: Economic Geology, v. 80, p. 126–147.

Farías, M., Charrier, R., Carretier, S., Martinod, J., Fock, A., Campbell, D., Cáceres, J., and Comte, D., 2008, Late Miocene high and rapid surface uplift and its erosional response in the Andes of central Chile (33°–35°S): Tectonics, v. 27, TC1005, doi:10.1029/2006TC002046.

Fournier, R.O., 1999, Hydrothermal processes related to movement of fluid from plastic into brittle rock in the magmatic-epithermal environment: Economic Geology, v. 94, p. 1193–1211.

Franchini, M., Impiccini, A., Lentz, D., Ríos, J., O'Leary, S., Pons, J., and Schalamuk, A., 2011, Porphyry to epithermal transition in the Agua Rica polymetallic deposit, Catamarca, Argentina: An integrated petrologic analysis of ore and alteration parageneses: Ore Geology Reviews, v. 41, p. 49–74.

Franchini, M., Impiccini, A., Beaufort, D., Patrier, P., Anderson, C.G., and Pons, J., 2012, Mineral assemblages and distribution of phyllosilicates composition along the main section of the Agua Rica deposit, Catamarca, Argentina. Implications for future mine development: Applied Clay Science, v. 67, p. 61–71.

Gammons, C.H., and Williams-Jones, A.E., 1997, Chemical mobility of gold in the porphyry-epithermal environment: Economic Geology, v. 92, p. 45–59.

Gans, C.R., Beck, S.L., Zandt, G., Gilbert, H., Alvarado, P., Anderson, M., and Linkimer, L., 2011, Continental and oceanic crustal structure of the Pampean flat slab region, western Argentina, using receiver function analysis: New high-resolution results: Geophysical Journal International, v. 186, p. 45–58.

Gatzoubaros, M., von Quadt, A., Gallhofer, D., and Rey, R., 2014, Magmatic evolution of pre-ore volcanics and porphyry intrusives associated with the Altar Cu-porphyry prospect, Argentina: Journal of South American Earth Sciences, v. 55, p. 58–82.

Giambiagi, L.B., and Ramos, V.A., 2002, Structural evolution of the Andes in a transitional zone between flat and normal subduction (33°30'–33°45'S), Argentina and Chile: Journal of South American Earth Sciences, v. 15, p. 101–116.

Goldstein, R.H., and Reynolds, T.J., 1994, Systematics of fluid inclusions in diagenetic minerals: Society of Sedimentary Geology, SEPM Short Course 31, 199 p.

Gustafson, L.B., and Hunt, J.P., 1975, The porphyry copper deposit al El Salvador, Chile: Economic Geology, v. 70, p. 857–912.

Gustafson, L.B., and Quiroga, J., 1995, Patterns of mineralization and alteration below the porphyry copper orebody at El Salvador, Chile: Economic Geology, v. 90, p. 2–16.

Hedenquist, J.W., 1987, Volcanic-related hydrothermal systems in the Circum-Pacific basin and their potential for mineralisation: Mining Geology (Kozan Chishitsu), v. 37, p. 347–364.

Hedenquist, J.W., Arribas, Jr., A., and Reynolds, T.J., 1998, Evolution of an intrusion- centered hydrothermal system: Far Southeast-Lepanto porphyry and epithermal Cu-Au deposits, Philippines: Economic Geology, v. 93, p. 373–404.

Hedenquist, J., Arribas, A., and Gonzales-Urien, E., 2000, Exploration for epithermal gold deposits: Society of Economic Geology Reviews, v. 13, p. 245–277.

Heinrich, C.A., 2005, The physical and chemical evolution of low- to medium-salinity magmatic fluids at the porphyry to epithermal transition: A thermodynamic study: Mineralium Deposita, v. 39, p. 864–889.

Heinrich, C., Driesner, T., Stefánsson, A., and Seward, T.M., 2004, Magmatic vapor contraction and the transport of gold from porphyry to epithermal ore deposits: Geology, v. 39, p. 761–764.

Huang, R., and Audétat, A., 2012, The titanium-in-quartz (TitaniQ) thermobarometer: A critical examination and re-calibration: Geochimica et Cosmochimica Acta, v. 84, p. 75–89.

Jochum, K.P., Weis, U., Stoll, B., Kuzmin, D., Yang, Q., Raczek, I., Jacob, D., Stracke, A., Birbaum, K., Frick, D., Günther, D., and Enzweiler, J., 2011, Determination of reference values for NIST SRM 610-617 glasses following ISO guidelines: Geostandards and Geoanalytical Research, v. 35, p. 397–429.

Jordan, T.E., Burns, W., Vega, R., Pángaro, F., Copeland, P., Kelley, S., and Mpodozis, C., 2001, Extension and basin formation in the Southern Andes caused by increased convergence rate: A Mid-Cenozoic trigger for the Andes: Tectonics, v. 20, p. 308–324.

Kay, S.M., and Mpodozis, C., 2002, Magmatism as a probe to the Neogene shallowing of the Nazca plate beneath the modern Chilean flat-slab: Journal of South American Earth Sciences, v. 15, p. 39–57.

Kay, S.M., Godoy, E., and Kurtz, A., 2005, Episodic arc migration, crustal thickening, subduction erosion, and magmatism in the south-central Andes: Geological Society of America Bulletin, v. 117, p. 67–88.

Kehayov, R., Bogdanov, K., Fanger, L., von Quadt, A., Pettke, T., and Heinrich, C.A., 2003, The fluid chemical evolution of the Elatiste porphyry Cu-Au-PGE deposit, Bulgaria: Mineral exploration and sustainable development: Rotterdam, Millpress, p. 1173–1176.

Kennedy, G.C., 1950, A portion of the system silica-water: Economic Geology, v. 45, p. 629–653.

Landtwing, M., Pettke, T., Halter, W., Heinrich, C., Redmond, P., Einaudi, M., and Kunze, K., 2005, Copper deposition during quartz dissolution by cooling magmatic-hydrothermal fluids: The Bingham porphyry: Earth and Planetary Science Letters, v. 235, p. 229–243.

Lindsay, D., Zentilli, M., and Rojas, J., 1995, Evolution of an active ductile to brittle shear system controlling mineralization at the Chuquicamata porphyry copper deposit, northern Chile: International Geology Review, v. 37, p. 945–958.

Maksaev, V., Munizaga, F., Zentilli, M., and Charrier, R., 2009, Fission track thermochronology of Neogene plutons in the Principal Andean Cordillera of central Chile (33–35°S): Implications for tectonic evolution and porphyry Cu-Mo mineralization: Andean Geology, v. 36, p. 153–171.

Marek, J.M., 2014, Estimated mineral resources Altar and Quebrada de la Mina deposits, San Juan Province Argentina: Prepared by Independent Mining Consultants, Inc., for Stillwater Mining Company, Technical Report, 169 p.

Masterman, G.J., Cooke, D.R., Berry, R.F., Walshe, J.L., Lee, A.W., and Clark, A.H., 2005, Fluid chemistry, structural setting, and emplacement history of the Rosario Cu-Mo porphyry and Cu-Ag-Au epithermal veins, Collahuasi district, northern Chile: Economic Geology, v. 100, p. 835–862.

Maydagán, L., 2012, El Prospecto de Cu-(Au-Mo) Altar (31º 29'LS, 70º28'LO), San Juan: Unpublished Ph.D thesis, Bahía Blanca, Argentina, Universidad Nacional del Sur, 340 p.

Maydagán, L., Franchini, M., Chiaradia, M., Pons, J., Impiccini, A., Toohey, J., and Rey, R., 2011, Petrology of the Miocene igneous rocks in the Altar Region, Main Cordillera of San Juan, Argentina: A geodynamic model within the context of the Andean flat-slab segment and metallogenesis: Journal of South American Earth Sciences, v. 32, p. 30–48.

Maydagán, L., Franchini, M., Lentz, D., Pons, J., and McFarlane, C., 2013, Sulfide composition and isotopic signature of the Altar Cu-Au deposit, Argentina: Constraints on the evolution of the porphyry-epithermal system: Canadian Mineralogist, v. 51, p. 813–840.

Maydagán, L., Franchini, M., Chiaradia, M., Dilles, J., and Rey, R., 2014, Intrusion history of the Altar porphyry Cu-(Mo-Au) deposit (Argentina): A complex magmatic-hydrothermal system with evidence of recharge processes: Economic Geology, v. 109, p. 621–641.

McFarlane, C., and Luo, Y., 2012, U-Pb geochronology using 193 nm excimer LA-ICP-MS optimized for in situ accessory mineral dating in thin section: Geoscience Canada, v. 39, p. 158–172.

Meyer, C., Shea, E.P., Goddard, Jr., C.C., and Staff, 1968, Ore deposits at Butte, Montana, *in* Ridge, J.D., ed., Ore deposits of the United States: New York, American Institute of Mining, Metallurgical, and Petroleum Engineers, p. 1373–1416.

Moore, D.M., and Reynolds, R.J.R., 1997, X-ray diffraction and the identification and analysis of clay minerals: New York, Oxford University Press, 378 p.

Mpodozis, C., and Cornejo, P., 2012, Cenozoic tectonics and porphyry copper systems of the Chilean Andes: Society of Economic Geologists Special Publication 16, p. 329–360.

Müller, A., Armstrong, R., Herrington, R., and Seltmann, R., 2003, Characterization of quartz textures in porphyry copper ore deposits by scanning electron microscope-cathodoluminescence (SEM-CL): Mongolian Geoscientist, v. 21, p. 32–35.

Müller, A., Herrington, R., Armstrong, R., Seltmann, R., Kirwin, D., Stenina, N., and Kronz, A., 2010, Trace elements and cathodoluminescence of quartz in stockwork veins of Mongolian porphyry-style deposits: Mineralium Deposita, v. 45, p. 707–727.

Muñoz, M., Fuentes, F., Vergara, M., Aguirre, L., Nyström, J.O, Féraud, G., and Demant, A., 2006, Abanico East Formation: Petrology and geochemistry of volcanic rocks behind the Cenozoic arc front in the Andean Cordillera, central Chile (33°50'S): Revista Geológica de Chile 33, v. 1, p. 109–140.

Muntean, J.L., and Einaudi, M.T., 2001, Porphyry-epithermal transition: Maricunga belt, northern Chile: Economic Geology, v. 96, p. 743–772.

Ossandón, G., Fréraut, R., Gustafson, L.B., Lindsay, D.D., and Zentilli, M., 2001, Geology of the Chuquicamata mine: A progress report: Economic Geology, v. 96, p. 249–270.

Paton, C., Hellstrom, J., Paul, B., Woodhead, J., and Hergt, J., 2011, Iolite: Freeware for the visualisation and processing of mass spectrometric data: Journal of Analytical Atomic Spectrometry, v. 26, p. 2508–2518.

Peregrine Metals Ltd., 2011, Altar Project, San Juan Province, Argentina, NI 43-101 Technical Report: Peregrine Metals Ltd., 151 p., www.peregrinemetals.com.

Perelló, J., Rojas, N., Devaux, C., Fava, L., Etchart, E., and Harman, P., 1998, Discovery of the Agua Rica porphyry Cu-Mo-Au deposit, Catamarca Province, northwestern Argentina. Part II: Geology, *in* Porter, T.M., ed., Porphyry and hydrothermal copper and gold deposits: A global perspective: Adelaide, Australian Mineral Foundation, p. 117–132.

Perelló, J., Brockway, H., and Martini, R., 2004, Discovery and geology of the Esperanza porphyry copper-gold deposit, Antofagasta Region, northern Chile: Society of Economic Geologists Special Publication 11, p. 167–186.

Perelló, J., Sillitoe, R.H., Mpodozis, C., Brockway, H., and Posso, H., 2012, Geologic setting and evolution of the porphyry copper-molybdenum and copper-gold deposits at Los Pelambres, central Chile: Society of Economic Geologists Special Publication 16, p. 79–104.

Proffett, J.M., 2003, Geology of the Bajo de la Alumbrera porphyry copper-gold deposit, Argentina: Economic Geology, v. 98, p. 1535–1574.

Pudack, C., Halter, W.E., Heinrich, C.A., and Pettke, T., 2009, Evolution of magmatic vapor to gold-rich epithermal liquid: The porphyry to epithermal transition at Nevados de Famatina, northwest Argentina: Economic Geology, v. 104, p. 449–477.

Roedder, E., 1984, Fluid inclusions: Reviews in Mineralogy, v. 12, 644 p.

——1992, Fluid Inclusion evidence for fluid immiscibility during magmatic differentiation: Geochimica et Cosmochimica Acta, v. 56, p. 5–20.

Rusk, B., 2012, Cathodoluminescnce and trace elements in hydrothermal quartz, *in* Götze, J., and Möckel, R., eds., Quartz: Deposits, mineralogy and analytics: Berlin, Heidelberg, Springer, p. 307–329.

Rusk, B.G., and Reed, M.H., 2002, Scanning electron microscope-cathodoluminescence of quartz reveals complex growth histories in veins from the Butte porphyry copper deposit, Montana: Geology, v. 30, p. 727–730.

Rusk, B.G., Reed, M.H., Dilles, J.H., and Kent, A.J.R., 2006, Intensity of quartz cathodoluminescence and trace-element content in quartz from the porphyry copper deposit at Butte, Montana: American Mineralogist, v. 91, p. 1300–1312.

Rusk, B.G., Reed, M.H., and Dilles, J.H., 2008a, Fluid inclusion evidence for magmatic-hydrothermal fluid evolution in the porphyry copper-molybdenum deposit at Butte, Montana: Economic Geology, v. 103, p. 307–334.

Rusk, B.G., Miller, B.J., and Reed, M.H., 2008b, Fluid inclusion evidence for the formation of Main stage polymetallic base-metal veins, Butte, Montana, USA: Tucson, Arizona Geological Society, Digest 22, p. 573–581.

Rusk, B., Koenig, A., and Lowers, H., 2011, Visualizing trace element distribution in quartz using cathodoluminescence, electron microprobe, and laser ablation-inductively coupled plasma-mass spectrometry: American Mineralogist, v. 96, p. 703–708.

Seedorff, E., Dilles, J., Proffett, J., and Einaudi, M., 2005, Porphyry deposits: Characteristics and origin of hypogene features: Economic Geology 100th Anniversary Volume, p. 251–298.

Seward, T.M., 1981, Metal complex formation in aqueous solutions at elevated temperatures and pressures, *in* Rickard, D.T., and Wickman, F.E., eds., Chemistry and geochemistry of solutions at elevated temperatures and pressures: Oxford, England, Pergamon Press, p. 113–132.

Sillitoe, R.H., 1983, Enargite-bearing massive sulfide deposits high in porphyry copper systems: Economic Geology, v. 78, p. 348–352.

——1994, Erosion and collapse of volcanoes: Causes of telescoping in intrusion-centered ore deposits: Geology, v. 22, p. 945–948.

Sillitoe, R.H., and Hedenquist, J.W., 2003, Linkages between volcanotectonic settings, ore-fluid compositions, and epithermal precious metal deposits: Society of Economic Geologists Special Publication 10, p. 315–343.

Sillitoe, R.H., and Khan, S.N., 1977, Geology of the Saindak porphyry copper deposit, Pakistan: Institution of Mining and Metallurgy Transactions, v. 86, p. 27–42.

Simmons, S., White, N., and John, D., 2005, Geological characteristics of epithermal precious and base metal deposits: Economic Geology 100th Anniversary Volume, p. 485–522.

Stoffregen, R.E., 1987, Genesis of acid-sulfate alteration and Au-Cu-Ag mineralization at Summitville, Colorado: Economic Geology, v. 82, p. 1575–1591.

Thomas, J., Watson, E., Spear, F., Shemella, P., Nayak, S., and Lanzirotti, A., 2010, TitaniQ under pressure: The effect of pressure and temperature on the solubility of Ti in quartz: Contributions to Mineralogy and Petrology, v. 160, p. 743–759.

Ulrich, T., and Heinrich, C.A., 2001, Geology and alteration geochemistry of the porphyry Cu-Au deposit at Bajo de la Alumbrera, Argentina: Economic Geology, v. 96, p. 1719–1742.

Ulrich, T., Günther, D., and Heinrich, C.A., 2001, The evolution of a porphyry Cu-Au deposit, based on LA-ICP-MS analysis of fluid inclusions: Bajo de la Alumbrera, Argentina: Economic Geology, v. 96, p. 1743–1774.

Wilkinson, J., Vry, V., Spencer, E.T., and Seguel, J., 2013, Fluid evolution in a super-giant porphyry Cu-Mo deposit: El Teniente, Chile: Society for Geology Applied to Mineral Deposits (SGA), SGA Biennial Meeting, 12th, 2013, Uppsala, Sweden, Proceedings, p. 906–909.

Yáñez, G., Ranero, G., von Huene, R., and Diaz, J., 2001, Magnetic anomaly interpretation across a segment of the southern central Andes (32°–34°S): Implications on the role of the Juan Fernández Ridge in the tectonic evolution of the margin during the upper tertiary: Journal of Geophysical Research, v. 106, p. 6325–6345.

Zwahlen, C., Cioldi, S., Wagner, T., Rey, R., and Heinrich, C., 2014, The porphyry Cu-(Mo-Au) deposit at Altar (Argentina): Tracing gold distribution by vein mapping and LA-ICP-MS mineral analysis: Economic Geology, v. 109, p. 1341–1358.